Moist convection drives an upscale energy transfer at Jovian high latitudes

Lia Siegelman[1*], Patrice Klein[2,3], Andrew P. Ingersoll[2], Shawn P. Ewald[2], William R. Young[1], Annalisa Bracco[4], Alessandro Mura[5], Alberto Adriani[5], Davide Grassi[5], Christina Plainaki[6], and Giuseppe Sindoni[6]

[1]Scripps Institution of Oceanography, University of California, San Diego, La Jolla, CA 92037, USA
[2]Division of Geological and Planetary Sciences, California Institute of Technology, Pasadena, CA 91106, USA
[3]Laboratoire de Météorologie dynamique, Ecole Normale Supérieure, 75005 Paris, France
[4]School of Earth and Atmospheric Sciences, Georgia Institute of Technology, Atlanta, GA 30332, USA
[5]Istituto Nazionale di AstroFisica – Istituto di Astrofisica e Planetologia Spaziali (INAF-IAPS), Rome, Italy
[6]Agenzia Spaziale Italiana (ASI), Via del Politecnico snc, 00133 Rome, Italy
[*]lsiegelman@ucsd.edu

Abstract

Jupiter's atmosphere is one of the most turbulent places in the solar system. While lightning and thunderstorm observations point to moist convection as a small-scale energy source for Jupiter's large-scale vortices and zonal jets, it has never been demonstrated due to the coarse resolution of pre-Juno measurements. Since 2017, the Juno spacecraft discovered that Jovian high-latitudes host a cluster of large cyclones (diameter of $\sim$ 5,000 km each) associated with intermediate ($\sim$ 1,600–500 km) and smaller-scale vortices and filaments ($\sim$ 100 km). Here, we analyze Juno-infrared images with an unprecedented high-resolution of 10 km. We unveil a new dynamical regime associated with a significant energy source of convective origin that peaks at 100 km–scales and in which energy gets subsequently transferred upscale to the large circumpolar and polar cyclones. While this energy route has never been uncovered on another planet, it is surprisingly consistent with idealized studies of rapidly rotating Rayleigh-Bénard convection, lending robust theoretical support to our analyses. This energy route is expected to enhance the heat transfer from Jupiter's hot interior to its troposphere and may also be relevant to the Earth's atmosphere, helping us better understand the dynamics of our own planet.

Main

The Jovian InfraRed Auroral Mapper (JIRAM) onboard Juno, operating at 4.8-μm and capturing NH_3 clouds[1,2], revealed a whole new set of weather phenomena present at Jovian high latitudes[1,3]. In contrast to mid-latitude cloud bands and zonal jets, the dominant features are numerous vortices of varying size (Fig. 1), including a cluster of large cyclonic vortices located at about $\pm 83°$ (8 in the north and 5 in the south) surrounding a single polar cyclone. These cyclones have a diameter of $\sim 5,000$ km, peak speeds of 100 m s^{-1}, a fast rotation period of $\sim$ 10 hours and have endured since their discovery in 2017[1,3,4]. Intermediate-scale cyclones and anticyclones, with a diameter of $\sim 1,000$ km and less, have a similar rotation period. The smallest observable vortices and filaments ($<$ 100 km) survive a couple of hours to several days only[3] and are the signature of an intense cloud activity[3,4] (Fig. 1). Lightnings reported at northern latitudes in recent studies[5–7], especially above the 2-bar level[7], point to moist convection within NH_3 clouds as a powerful source of energy in Jupiter's polar regions. However, even though the dynamical link between small-scale moist convection and large-scale vortices has been investigated at high latitudes in recent modeling studies[8–11], it has never been derived from observations.

Here, we investigate this link using high resolution infrared images taken by JIRAM at the north pole of Jupiter on February 2, 2017, from which two complementary datasets are derived. First, we use wind velocities (Extended Data Fig. 1) derived by tracking clouds in sequence of infrared images (see paper[4] for the methodology) in a domain greater than $7,000 \times 20,000$ km (black rectangle in Fig. 1), where overlapping observations over short intervals are available. The wind field has a resolution of 10 km, which is slightly higher than previous measurements[12]. Second, the optical depth, defined as $\log(I_0/I)$, with I the brightness and $I_0 = 0.55946$ W m^{-2} the maximum brightness, is directly derived from the infrared measurements[3] with the same resolution as the wind field (Figure 2a). Optical depth is related to variations in cloud thickness such that a thick cloud produces a high optical depth[3,13].

The analysis of these two unique datasets using a theoretical framework (the surface quasi-geostrophy (SQG) framework[14–18],

described in the moist convection section) allows us to uncover a new dynamical regime on Jupiter, which highlights the key role played by moist convection at Jovian high latitudes. Surprisingly, this regime is reminiscent of idealized studies of rapidly rotating Rayleigh-Bénard convection (R^3BC)[19–23], laboratory experiments[24] and may even resembles parts of the Earth's atmosphere[25–27].

Dynamical context

We analyze the properties of the wind measurements in terms of kinetic energy (KE), relative vorticity (ζ, i.e., the local rate of spin of a vortex, see Methods) and horizontal divergence (χ, see Methods). The magnitude of ζ (Extended Data Fig. 2a) and χ (Extended Data Fig. 2b) reaches the local spin rate of the planet ($f = 3.5 \times 10^{-4}$ s^{-1}, also called the Coriolis parameter), which is one fold higher than previous estimates[28]. First, we use a suite of spectral analyses (see Methods) to investigate how KE, ζ and χ are distributed among length scales and what their spectral characteristics tell us about the underlying dynamical regime (see Methods). The KE spectrum (Fig. 3a) exhibits two distinct scale ranges separated by a conspicuous spectral slope discontinuity: scales larger than 1,600 km are characterized by a steep slope in k^{-3} (with k the wavenumber), whereas scales smaller than 1,600 km are characterized by a shallower slope in $k^{-4/3}$. This discontinuity is even more striking in ζ's power spectrum (blue curve in Fig. 3b) since the slope changes sign at 1,600 km. Second, we retrieve the physical patterns captured by each scale range using a spectral filter (see Methods). As expected, the ζ-field associated with the k^{-3} scale range comprise the large vortices, including the persistent circumpolar and polar cyclones as well as one large anticyclone (Fig. 2b). Since χ-spectral amplitude is a lot smaller than ζ-spectral amplitude in this scale range (Fig. 3b), large scales are likely governed by 2-D turbulence[29]. The Rossby number, defined as Ro = ζ/f reaches 0.5 and its distribution is positively skewed (Extended Data Fig. 3b), confirming the overwhelming dominance of the large cyclones in the k^{-3} scale range. In contrast, the $k^{-4/3}$ scale range (length scales of ~100–1,600 km) includes numerous cyclones, anticyclones and elongated filaments embedded in-between the vortices (Extended Data Fig. 2a). Unlike the k^{-3} scale range, χ and ζ's variance are of the same order of magnitude, and are even equal for scales smaller than 300 km (Fig. 3b,c), suggesting that vortices in this scale range are forced by vertical motions and hence that their dynamics is 3-D[30]. Finally, the Ro distribution is only slightly negatively skewed (Extended Data Fig. 3c), highlighting the absence of a cyclone-anticyclone preference in the $k^{-4/3}$ scale range.

Overall, the wind measurements' analysis highlights a turbulent regime, which involves two classes of vortices separated by a conspicuous spectral slope discontinuity (blue curve in Fig. 3a,b); large-scale vortices for which the surface dynamics is likely driven by horizontal motions and smaller vortices and filaments affected by vertical motions. However, vorticity and divergence diagnosed from the wind measurements contain small-scale noise ($\lesssim$ 100 km, Extended Data Fig. 2) as their computation involves both spatial and temporal derivatives. This noise prevents us from analyzing the link between small-scale features and large-scale vortices solely from the wind measurements.

Moist convection is a KE source at 100 km–scales

We use the information provided by the optical depth anomaly, τ, in combination with the wind measurements. Positive values of τ correspond to thick clouds (i.e., updrafts) and negative values to no or thin clouds (i.e., downdrafts)[3,13,31]. Thus, τ can be interpreted as the signature of vertical motions and therefore as a vertical scale. Based on the assumption that cloud thickness is an indicator of tropopause-height anomalies (as for the Earth's tropopause[15]), tropopause-height anomalies are estimated as $h = H_0.\tau$, with H_0 the length-scale of tropopause-level anomalies. Then, τ can be interpreted in terms of available potential energy (APE) defined as N^2h^2, with N the Brunt-Väissälä frequency (see Methods). APE and KE spectra have the same slope ($k^{-4/3}$) for scales $< 1,600$ km, which is reminiscent of the dynamical SQG framework[14–18] (see Methods). In the next paragraph, we use this framework and focus on the $k^{-4/3}$ scale range to better understand the properties of the intermediate and small-scale vortices.

In SQG, APE and KE spectra are identical, which leads to simple relationships between horizontal motions and h[18]. As the SQG framework is relevant for the Earth's tropopause[14,15,17,18,26], we assume that it also applies to Jupiter. We adjust the APE's spectrum amplitude to match that of KE for scales $< 1,600$ km by taking N constant and equal to $N = 4.10^{-3}$ s^{-1} in Jupiter's upper troposphere[32] and choosing $H_0 = 9$ km (Fig. 3a). Using SQG properties, a relative vorticity can be directly diagnosed from τ (equation (10) in Methods). This relative vorticity field, ζ_τ, is displayed in Fig 2c. As expected, ζ and ζ_τ's spectra overlap in the $k^{-4/3}$ scale range (orange and blue curves in Fig. 3b). To validate our assumption that SQG applies in the $k^{-4/3}$ scale range, we now compare ζ and ζ_τ in physical space after application of a conservative band-pass filter that retains only length-scales between 250 and 1,600 km (see Methods and Extended Data Fig. 4b,c for the filtered fields). Although ζ is noisier than ζ_τ (see Methods), the correspondence between the two fields is striking, especially where ζ is well resolved. For instance, the streamer between the two anticyclones is characterized by a filament of negative relative vorticity surrounded by two filaments of positive relative vorticity in both ζ and ζ_τ (black polygon in Extended Data Fig. 4b,c). The relationship between ζ and ζ_τ is corroborated by the scatterplots in Extended Data Fig. 5, confirming the existence of a SQG regime and

the fact that τ can interpreted in terms of tropopause-level anomalies, with H_0 the typical depth scale. In addition, the good match between ζ and ζ_τ confirms the positive correlation between anticyclonic vorticity and positive cloud thickness anomaly (equation (10) in Methods). At last, an estimation of the convective APE (CAPE)[33,34] within NH_3 clouds leads to an order of magnitude similar to our APE, confirming its convective origin (see Methods).

Convection within clouds is known to be associated with updrafts, producing positive divergence and anticyclonic vorticity at the cloud top[31,35]. This is consistent with our dynamical analysis, which implies that thick clouds (i.e., positive optical depth anomaly τ) are associated with anticyclonic vorticity and the fact that ζ_τ is negatively correlated with χ (Extended Data Fig. 6). Furthermore, χ has the same magnitude as the divergence estimated from CAPE within clouds (see Methods) and as the ones reported for cloud convection in Jupiter[34,36]. Taken together, it indicates that thick clouds are associated with positive divergence and anticyclonic vorticity, consistent with a convective origin. To double-check this result, we also investigate the direct relation between τ and χ (Extended Data Figs. 4 and 7), which confirms the positive correlation between cloud thickness and divergence, lending further support to moist convection at Jovian high latitudes. Moist convection is most significant at 100 km–scales, as suggested by the maxima of ζ_τ, ζ and χ's spectra (Fig. 3b).

KE and APE spectra greatly differ for scales larger than 1,600 km (Fig. 3a). The APE spectrum (orange curve in Fig. 3a) has a shallower slope and a much smaller variance than the KE spectrum (blue curve in Fig. 3a). In addition, the divergence is weak in this range (Fig. 3b). Taken together, it implies that vortices in the k^{-3} scale range are not directly impacted by clouds (see Methods' section "Dynamics in the k^{-3} scale range"), consistent with a character and generation mechanism independent of tropopause-level forcing[2]. A natural follow up question that begs to be answered is: can moist convection, through vortices in the $k^{-4/3}$ scale range, account for the emergence and persistence of the large cyclones present at Jovian high latitudes in the k^{-3} scale range? This is addressed in the next section.

Upscale energy transfer

Here, we diagnose the KE transfer across scales to understand how small-scale moist convection impacts the large cyclones. The KE transfer, KE_{adv}, is derived from the momentum equations and computed from the wind measurements (see Methods). A negative (positive) value of $KE_{adv}(k)$ indicates a KE loss (gain) at the wavenumber k. Fig. 4a reveals that scales smaller than 215 km, where the KE source due to convection is the most significant, lose KE. On the other hand, larger scales up to about 5,000 km gain KE. This indicates an upscale KE transfer in both the k^{-3} and $k^{-4/3}$ scale ranges, from the smallest observable vortices ($<$100 km) up to the large cyclones ($\sim 5,000$ km). Note that while the zero-crossing value of 215 km (Fig. 4a) is weakly sensitive to the data processing and can vary between 100 and 400 km (Extended Data Fig. 11), the upscale energy transfer up to the large cyclones' scale is a robust feature of the flow. In addition, a downscale enstrophy (i.e., the relative vorticity squared) transfer is observed at all scales (Fig. 4b), consistent with an upscale energy transfer in classical theory of rotating turbulence[37]. Taken together, these results show that turbulence at Jovian high latitudes is forced by convection at 100 km–scales and that the resulting KE cascades upscale to the large circumpolar and polar cyclones. This upscale KE transfer is consistent with previous analyses of Jovian mid-latitudes for scales larger than $\sim$1,600 km[28] but has never been reported at smaller scales.

Our findings are remarkably consistent with recent idealized R^3BC studies[19–23], as well as with laboratory experiments[24] and numerical simulations of forced turbulence in a rotating frame[38] with generic small-scale forcing. All these studies reveal the existence of KE and APE spectra similar to those in Fig. 3a as well as an upscale KE transfer from small-scale forcing up to the large 2-D vortices. They further indicate that the upscale KE transfer is enhanced by a positive feedback loop whereby large-scale vortices organize intermediate and small-scale convective features. In other words, 2-D vortices organize 3-D vortices and filaments, themselves constraining the convection[39]. The noticeable spiral bands of relative vorticity and clouds around the polar vortex (Fig. 2a,c), as well as the aggregation of thick clouds within intermediate-scale anticyclones (Extended Data Fig. 5) is consistent with such positive feedback loop. For instance, the streamer of negative vorticity and thick clouds (Fig. 2a,c and Extended Data Fig. 4a,b) suggests that small-scale moist convection is organized by intermediate-scale vortices and filaments, with the latter being advected and stretched by the large cyclones. However, verifying these results in Jupiter would require a longer time series of observations than currently available.

Discussion

Our results show that moist convection at 100 km–scales is associated with an upscale energy transfer strengthening the large cyclones at Jovian high latitudes. This energy route is expected to increase the heat transfer between deep and hot interior layers and colder upper layers, where heat gets converted into KE[20–22,40], which is also consistent with deep convection and a deep extent of the large cyclones[41,42]. If this was the case, the presence of two convective regimes (a deep one responsible for the large cyclones and mostly forced from below, and a shallower one responsible for the smaller circulations and directly

linked to clouds and winds) would point to an explicit stratification in the upper portion of Jupiter's polar atmosphere. Other non-mutually exclusive mechanisms can also account for the genesis and persistence of the cluster of cyclones at Jupiter's poles. Cyclones are expected in the polar regions because of the β-effect, which forces cyclones (anticyclones) to drift poleward (equatorward)[43]. An estimation of the β-drift, or planetary Burger number[8], agrees with a regime comprised of multiple circumpolar cyclones[9,10] (see Methods). The stability of Jupiter's cluster of cyclones may also be explained by more complex vorticity dynamics[4,44,45].

This study contributes to our fundamental understanding of vortex dynamics and highlights a regime that has never been reported on another planet before using observations. The closest dynamical analogs in the solar system may well be some parts of the Earth's atmosphere[25,27]. Indeed, the mechanisms highlighted here could apply to the Earth's troposphere, as can be inferred from the Global Atmospheric Sampling Program (GASP) observations[25]. In close agreement with the Jovian wind measurements presented here, the GASP observations are characterized by a conspicuous KE spectrum with a k^{-3} slope for large scales and $k^{-5/3}$ for smaller scales[25,46]. The corresponding dynamical regime remains an open question[26,46,47], mainly because of the lack of 2-D observations, even though numerical studies point to moist convection as the leading mechanism[27,46,48]. The results of the present study highlight the power of combining high-resolution 2-D cloud observations with wind measurements, which, if applied to the Earth's atmosphere, should help us better understand the dynamics of our own planet.

References

1. Adriani, A. *et al.* Clusters of cyclones encircling jupiter's poles. *Nature* **555**, 216–219 (2018).
2. Mura, A. *et al.* Oscillations and stability of the Jupiter polar cyclones. *Geophys. Res. Lett.* e2021GL094235 (2021).
3. Adriani, A. *et al.* Two-year observations of the Jupiter polar regions by JIRAM on board Juno. *J. Geophys. Res. Planets* e2019JE006098 (2020).
4. Ingersoll, A. *et al.* Polygonal patterns of cyclones on Jupiter: Convective forcing and anticyclonic shielding. *Nat. Astron.* (in revision).
5. Baines, K. H. *et al.* Polar lightning and decadal-scale cloud variability on jupiter. *science* **318**, 226–229 (2007).
6. Brown, S. *et al.* Prevalent lightning sferics at 600 megahertz near jupiter's poles. *Nature* **558**, 87–90 (2018).
7. Becker, H. N. *et al.* Small lightning flashes from shallow electrical storms on jupiter. *Nature* **584**, 55–58 (2020).
8. O'Neill, M. E., Emanuel, K. A. & Flierl, G. R. Polar vortex formation in giant-planet atmospheres due to moist convection. *Nat. Geosci.* **8**, 523–526 (2015).
9. O'Neill, M. E., Emanuel, K. A. & Flierl, G. R. Weak jets and strong cyclones: Shallow-water modeling of giant planet polar caps. *J. Atmospheric Sci.* **73**, 1841–1855 (2016).
10. Brueshaber, S. R., Sayanagi, K. M. & Dowling, T. E. Dynamical regimes of giant planet polar vortices. *Icarus* **323**, 46–61 (2019).
11. Brueshaber, S. R. & Sayanagi, K. M. Effects of forcing scale and intensity on the emergence and maintenance of polar vortices on saturn and ice giants. *Icarus* **361**, 114386 (2021).
12. Grassi, D. *et al.* First estimate of wind fields in the Jupiter polar regions from JIRAM-Juno images. *J. Geophys. Res. Planets* **123**, 1511–1524 (2018).
13. Moriconi, M. *et al.* Turbulence power spectra in regions surrounding Jupiter's south polar cyclones from Juno/JIRAM. *J. Geophys. Res. Planets* **125**, e2019JE006096 (2020).
14. Blumen, W. Uniform potential vorticity flow: Part i. theory of wave interactions and two-dimensional turbulence. *J. Atmospheric Sci.* **35**, 774–783 (1978).
15. Juckes, M. Quasigeostrophic dynamics of the tropopause. *J. Atmospheric Sci.* **51**, 2756–2768 (1994).
16. Held, I. M., Pierrehumbert, R. T., Garner, S. T. & Swanson, K. L. Surface quasi-geostrophic dynamics. *J. Fluid Mech.* **282**, 1–20 (1995).
17. Hakim, G. J., Snyder, C. & Muraki, D. J. A new surface model for cyclone–anticyclone asymmetry. *J. atmospheric sciences* **59**, 2405–2420 (2002).
18. Lapeyre, G. Surface quasi-geostrophy. *Fluids* **2**, 7 (2017).

19. Julien, K., Rubio, A. M., Grooms, I. & Knobloch, E. Statistical and physical balances in low rossby number rayleigh–bénard convection. *Geophys. & Astrophys. Fluid Dyn.* **106**, 392–428 (2012).

20. Favier, B., Silvers, L. & Proctor, M. Inverse cascade and symmetry breaking in rapidly rotating boussinesq convection. *Phys. Fluids* **26**, 096605 (2014).

21. Guervilly, C., Hughes, D. & Jones, C. Large-scale vortices in rapidly rotating Rayleigh–Bénard convection. *J. Fluid Mech.* **758**, 407 – 435 (2014).

22. Guervilly, C., Hughes, D. W. & Jones, C. A. Large-scale-vortex dynamos in planar rotating convection. *J. Fluid Mech.* **815**, 333–360 (2017).

23. Novi, L., von Hardenberg, J., Hughes, D. W., Provenzale, A. & Spiegel, E. A. Rapidly rotating rayleigh-bénard convection with a tilted axis. *Phys. Rev. E* **99**, 053116 (2019).

24. Xia, H., Byrne, D., Falkovich, G. & Shats, M. Upscale energy transfer in thick turbulent fluid layers. *Nat. Phys.* **7**, 321–324 (2011).

25. Nastrom, G. & Gage, K. S. A climatology of atmospheric wavenumber spectra of wind and temperature observed by commercial aircraft. *J. atmospheric sciences* **42**, 950–960 (1985).

26. Tulloch, R. & Smith, K. A theory for the atmospheric energy spectrum: Depth-limited temperature anomalies at the tropopause. *Proc. Natl. Acad. Sci.* **103**, 14690–14694 (2006).

27. Waite, M. L. & Snyder, C. Mesoscale energy spectra of moist baroclinic waves. *J. Atmospheric Sci.* **70**, 1242–1256 (2013).

28. Young, R. M. & Read, P. L. Forward and inverse kinetic energy cascades in Jupiter's turbulent weather layer. *Nat. Phys.* **13**, 1135–1140 (2017).

29. Charney, J. G. Geostrophic turbulence. *J. Atmospheric Sci.* **28**, 1087–1095 (1971).

30. Vallis, G. K. *Atmospheric and oceanic fluid dynamics* (Cambridge University Press, 2017).

31. Bony, S. *et al.* Clouds, circulation and climate sensitivity. *Nat. Geosci.* **8**, 261–268 (2015).

32. Achterberg, R. K. & Ingersoll, A. P. A normal-mode approach to jovian atmospheric dynamics. *J. atmospheric sciences* **46**, 2448–2462 (1989).

33. Holton, J. R. *An introduction to dynamic meteorology*, vol. 88 of *International Geophysics Series* (Elsevier Academic Press, 2004).

34. Iñurrigarro, P. *et al.* Observations and numerical modelling of a convective disturbance in a large-scale cyclone in jupiter's south temperate belt. *Icarus* **336**, 113475 (2020).

35. Ingersoll, A., Gierasch, P., Banfield, D., Vasavada, A. & Team, G. I. Moist convection as an energy source for the large-scale motions in Jupiter's atmosphere. *Nature* **403**, 630–632 (2000).

36. Hueso, R. & Sánchez-Lavega, A. A three-dimensional model of moist convection for the giant planets: The Jupiter case. *Icarus* **151**, 257–274 (2001).

37. Rhines, P. B. Waves and turbulence on a beta-plane. *J. Fluid Mech.* **69**, 417–443 (1975).

38. Smith, L. M. & Waleffe, F. Transfer of energy to two-dimensional large scales in forced, rotating three-dimensional turbulence. *Phys. fluids* **11**, 1608–1622 (1999).

39. Rubio, A. M., Julien, K., Knobloch, E. & Weiss, J. B. Upscale energy transfer in three-dimensional rapidly rotating turbulent convection. *Phys. review letters* **112**, 144501 (2014).

40. Boffetta, G., Mazzino, A. & Musacchio, S. Rotating rayleigh-taylor turbulence. *Phys. Rev. Fluids* **1**, 054405 (2016).

41. Yadav, R. K., Heimpel, M. & Bloxham, J. Deep convection–driven vortex formation on jupiter and saturn. *Sci. advances* **6**, eabb9298 (2020).

42. Yadav, R. K. & Bloxham, J. Deep rotating convection generates the polar hexagon on saturn. *Proc. Natl. Acad. Sci.* **117**, 13991–13996 (2020).

43. Theiss, J. Equatorward energy cascade, critical latitude, and the predominance of cyclonic vortices in geostrophic turbulence. *J. physical oceanography* **34**, 1663–1678 (2004).

44. Gavriel, N. & Kaspi, Y. The number and location of Jupiter's circumpolar cyclones explained by vorticity dynamics. *Nat. Geosci.* (2021).

45. Li, C., Ingersoll, A. P., Klipfel, A. P. & Brettle, H. Modeling the stability of polygonal patterns of vortices at the poles of Jupiter as revealed by the Juno spacecraft. *Proc. Natl. Acad. Sci.* **117**, 24082–24087 (2020).

46. Burgess, B. H., Erler, A. R. & Shepherd, T. G. The troposphere-to-stratosphere transition in kinetic energy spectra and nonlinear spectral fluxes as seen in ecmwf analyses. *J. atmospheric sciences* **70**, 669–687 (2013).

47. Lindborg, E. A helmholtz decomposition of structure functions and spectra calculated from aircraft data. *J. Fluid Mech.* **762** (2015).

48. Hamilton, K., Takahashi, Y. O. & Ohfuchi, W. Mesoscale spectrum of atmospheric motions investigated in a very fine resolution global general circulation model. *J. Geophys. Res. Atmospheres* **113** (2008).

49. Adriani, A. *et al.* JIRAM, the Jovian infrared auroral mapper. *Space Sci. Rev.* **213**, 393–446 (2017).

50. Grassi, D. *et al.* Analysis of ir-bright regions of Jupiter in JIRAM-Juno data: Methods and validation of algorithms. *J. Quant. Spectrosc. Radiat. Transf.* **202**, 200–209 (2017).

51. Gierasch, P. *et al.* Observation of moist convection in Jupiter's atmosphere. *Nature* **403**, 628–630 (2000).

52. Lindal, G. F. *et al.* The atmosphere of Jupiter: An analysis of the voyager radio occultation measurements. *J. Geophys. Res. Space Phys.* **86**, 8721–8727 (1981).

53. Bender, C. M. & Orszag, S. A. *Advanced mathematical methods for scientists and engineers I: Asymptotic methods and perturbation theory* (Springer Science & Business Media, 2013).

54. Gottlieb, D. & Orszag, S. A. *Numerical analysis of spectral methods: theory and applications* (Society for Industrial and Applied Mathematics, 1977).

55. Savage, A. C. *et al.* Spectral decomposition of internal gravity wave sea surface height in global models. *J. Geophys. Res. Ocean.* **122**, 7803–7821 (2017).

56. Hua, B. L., McWilliams, J. C. & Klein, P. Lagrangian accelerations in geostrophic turbulence. *J. Fluid Mech.* **366**, 87–108 (1998).

57. Pedlosky, J. *Geophysical fluid dynamics*, vol. 710 (Springer, 1987).

58. Smith, K. S. & Vallis, G. K. The scales and equilibration of midocean eddies: Freely evolving flow. *J. Phys. Oceanogr.* **31**, 554–571 (2001).

59. Frisch, U. & Kolmogorov, A. N. *Turbulence: the legacy of A.N. Kolmogorov* (Cambridge university press, 1995).

Methods

Datasets

Infrared images

Infrared images are taken by JIRAM's imaging channel in the M band, which operates at 4.8-μm wavelength. These are images of the NH_3 clouds shielding the thermal emission of the planet at different viewing angles[2]. During the perijove 4 orbit, JIRAM performed a series of overlapping observations of the poles of Jupiter in the hours bracketing perijove. In this paper we consider only the north polar sequences because they provide better overlap among the images and shorter intervals between images than at the south pole (see Extended Data Table 1). Observations are taken on February 2, 2017 and have a resolution of $\sim$ 10 km.pixel^{-1}, depending on foreshortening and spacecraft motion. The images processing, from the raw data to the polar orthographic projected maps, is thoroughly described in paper[4]. However, briefly, the first step in the processing is to determine the precise location of each pixel on the planet. This is done with NAIF/SPICE data from the spacecraft and precise geometric calibration of the JIRAM instrument[49]. The second step is to map the brightness patterns onto a 10-km grided reference plane tangent to the planet at the pole. Mosaics are then assembled by combining 12 such infrared images separated by 30 seconds each. A total of 4 mosaics (i.e., 48 infrared images, see Extended Data Table 1) are analyzed, all yielding same results (Extended Data Figs. 8–10). The projected infrared images are provided in the Supplementary Information under filename *mapped brightness*. In the main text, we show the results for one typical mosaic (n02, Figure 2a), taken at mid-time between the two mosaics used to derive the wind field described below.

Wind measurements

Horizontal winds are computed by tracking cloud features between two overlapping infrared observations separated by 16 min using Tracker 3 software from JPL (see ref[4]) with a resolution of 10 km and an error of 2.1 m.s^{-1}. That dataset is filename *velocity vector* in the Supplementary Information. To remove remaining small-scale noise, we apply a butterworth filter of order 1 with a cutoff wavelength of 250 km. We analyze a total of 2 wind mosaics (derived from a total of 48 infrared images),

yielding similar results (Extended Data Figs. 8–10). In the main text, we show results for the area with broader coverage (Extended Data Fig. 1), using the mosaics n01 and n03. Note that using velocity vectors and infrared brightness maps projected onto a 15 km/pixel-grid like is done in ref[4] and yields similar results. An analysis to the error propagation indicates that the errors associated with the wind measurements is confined to scales less than ~ 50 km (Extended Data Figs. 12 and 13) and therefore does not impact the conclusions of our study.

Optical depth

JIRAM infrared brightness I is primarily governed by cloud opacity[50], with high I corresponding to thin clouds located at pressures of 1–5 bars (i.e. within warm regions at depth), and low I corresponding to thick clouds that can reach the tropopause at a pressure of about 0.3 bar (i.e., within colder upper regions)[3,51,52]. Thus, JIRAM observations are not taken along a constant pressure surface and cannot be directly converted into a potential temperature from which one can infer horizontal motions at the tropopause, as done by ref[15] for the Earth. Consequently, instead of directly using I, we use the optical depth, a proxy of cloud thickness[3,13]. The optical depth is computed as $\tau_a = \log(\mathrm{I}_0/\mathrm{I})$, with $\mathrm{I}_0 = 0.55946$ W.m^{-2} the maximum brightness measured in the infrared mosaic n02 displayed in Fig. 2a, following refs[3,13]. In this study, we define the optical depth anomaly τ as $\tau = \tau_a - \overline{\tau_a}$, with $\bar{.}$ denoting the domain average.

Spectral methods

In this paper, all the computations are done in spectral space, which allow us to easily and accurately isolate different scales ranges[53]. Before taking the Fourier transform of any given variable, we apply two steps. First, we make the variable doubly periodic by applying a mirror symmetry in the x and y directions. Performing spectral analyses in a doubly-periodic domain considerably improves the result's accuracy compared to windowing methods, which damp both the large and small scales and can change the amplitude and slope of a power spectra density[54]. Second, the variable is detrended by subtracting the mean value.

Wavenumber spectrum

For a given doubly-periodic and detrended variable ϕ, we first compute a discrete 2-D fast Fourier transform $\widehat{\phi}(k_x,k_y)$, with k_x and k_y the wavenumbers in the x and y direction, and then we compute a 1D spectral density $|\widehat{\phi}(k)|^2$ from the 2-D spectrum, with k is the isotropic wave number defined as $k = \sqrt{k_x^2 + k_y^2}$, following a standard procedure described in ref[55].

Butterworth filter

Throughout the paper, we apply a low-pass Butterworth filter to the wind measurements to remove the remaining small-scale noise. After experimenting, we find that a filter of order 1 with a cutoff wavenumber of 250 km produces the best results in terms of the signal to noise ratio. We use the spectral characteristics of τ to infer the upper bound of the spectral variance at the smallest scales. To do so, $\hat{\zeta}$ does not exceed $\hat{\zeta}_\tau$ (defined below) for scales smaller than 100 km where most of the wind measurements' noise associated with taking the temporal derivative between two infrared observations is located. Note that we applied a Butterworth filter of order 2 and cutoff wavenumber of 500 km to the wind field in Extended Data Fig. 1 for visualization purposes.

Band pass filter

A band-pass filter is implemented in spectral space and retains a range of length-scales by setting the wavenumbers outside of this range to zero. In Extended Data Figs. 4–7, we apply a band pass filter that retains length scales between 250 and 1,600 km (i.e., wavenumbers between 6.10^{-4} cpkm and 4.10^{-3} cpkm). A sensitivity analysis to these wavenumbers was performed and results remain unchanged when scales smaller than 250 km are included (not shown). In Fig. 2, we apply a low-pass (panel b) and high-pass (panel c) version of this filter with a cutoff at 6.10^{-4} cpkm (i.e., at the spectral slope discontinuity shown in Fig. 3ab).

Relative vorticity and horizontal divergence

Relative vorticity $\hat{\zeta}$ and horizontal divergence $\hat{\chi}$ are computed in spectral space from horizontal wind measurements $\hat{u}$ and $\hat{v}$ as:

$$\hat{\zeta} = -i\,(k_y\,\hat{u} + k_x\,\hat{v}) \;\text{ and }\; \hat{\chi} = i\,(k_x\,\hat{u} + k_y\,\hat{v}),$$

with $i^2 = -1$. Note that the physical fields ζ and χ shown in Extended Data Fig. 2 are retrieved from the inverse 2-D fast Fourier transform of $\hat{\zeta}$ and $\hat{\chi}$, respectively. In addition, the computation of $\zeta = v_x - u_y$ and horizontal divergence $\chi = u_x + v_y$, with subscripts denoting partial derivative, is done in physical space in ref[4] and yields comparable results.

Rossby number

Taking the divergence of the momentum equations and assuming that the divergence's time derivative and friction terms are negligible at leading order, leads to[30]:

$$f\zeta - \nabla_h.(\mathbf{u}_h.\nabla_h\,\mathbf{u}_h) - \Delta_h P = 0, \tag{1}$$

with ∇_h the horizontal gradient operator, Δ_h the horizontal Laplacian operator, $\mathbf{u}_h$ the horizontal velocity vector and P the pressure. The Rossby number, defined as $\mathrm{Ro} \equiv \frac{U}{fL}$, with U and L respectively a velocity and length scales[30], quantifies in equation (1) the relative importance of the Coriolis term (i.e. $f\zeta$) compared to the nonlinear term. A dimensional analysis of equation (1) indicates that there is a balance between the Coriolis and pressure terms for $\mathrm{Ro} << 1$, called the geostrophic balance. For $\mathrm{Ro} \sim 1$, the balance also involves the nonlinear terms, called the gradient wind balance. In this study we estimate the Rossby number as $\mathrm{Ro} = \zeta/f$. The vortices at Jovian high latitudes have $\mathrm{Ro} \sim 1$, indicating that nonlinear terms and therefore nonlinear vortex interactions are significant.

Available potential energy

Tropopause level anomalies, h, are related to the optical depth anomaly, τ, via $h = H_0\,\tau$, with H_0 a scale depth of tropopause level anomalies. In the atmosphere, APE is defined as[15,30] $\left(g\frac{\Theta}{\Theta_0}\right)^2 \frac{1}{N^2}$, with g the gravitational constant, Θ the potential temperature taken on a constant pressure surface, Θ_0 the reference potential temperature and N^2 the squared Brunt-Väissälä frequency defined as $g\frac{\overline{\Theta_z}}{\Theta_0}$. As the potential temperature is unknown (see Methods section "optical depth"), we use a first order Taylor series expansion $g\frac{\Theta}{\Theta_0} \sim N^2 h$, yielding:

$$\mathrm{APE} = N^2 h^2\ . \tag{2}$$

τ is thus related to the APE via $h = H_0\tau$, with $H_0 = 9$ km and $N = 4.10^{-3}$ s^{-1} chosen such that KE and APE spectra are equal in the $k^{-4/3}$ scale range. N has been chosen from ref[32], yielding a value of $H_0 = 9$ km. Using these values yields APE = 1,296 m^{2}s^{-2}. Note that N might be slightly different at the pole, which in turn would change H_0, without however affecting our computations.

We suggest interpreting APE in terms of convective APE (CAPE)[33] in order to assign moist convection to condensation process within clouds[34]. CAPE = $gZ\frac{\delta T}{<T>}$, with δT the temperature difference between heated parcels and their background, Z the vertical length scale of the path followed by ascending parcels and $< T >$ the background mean temperature[33,34]. We use the values provided by ref[34] for NH_3 clouds: $< T >= 130$ K at 0.5 bar, $Z = 40$ km (from 0.1 to 1 bar) and $\delta T = 0.3$ K. This leads to CAPE = 2,612 m^{2}s^{-2}, a value close to our APE estimate. Note that the values for H_2O clouds yield a CAPE's magnitude ten times larger. As such, our CAPE estimation validates equation (2) and confirms that APE has a convective origin within NH_3 clouds.

In addition, using the relation CAPE = $w_{max}^2/2$ and $Z = 40$ km (ref[34]), yields an upper bound for the divergence within clouds of $w_{max}/Z \sim 7.10^{-4}$s^{-1}. This divergence value is consistent with χ estimated from the wind measurements as well as with modelling results[34,36].

Note that if we define a streamfunction $\psi = fP$, with P the pressure (as done in the next section), the hydrostatic approximation yields $\frac{\partial\psi}{\partial z} = \frac{g}{f}\frac{\Theta}{\Theta_0}$. APE can then be written as:

$$\mathrm{APE} = \frac{f^2}{N^2}\left(\frac{\partial\psi}{\partial z}\right)^2 \tag{3}$$

The quasi-geostrophic framework

The quasi-geostrophic (QG) framework is useful to study the dynamics of a flow field of $\mathrm{Ro} \sim O(1)$ despite relying on a small Ro approximation[30]. In particular, this framework has been successfully used to study thermal convection in the limit of rapid rotation[39], reminiscent of the observations presented here. In the QG framework, potential vorticity (PV) is conserved along a Lagrangian trajectory and the PV anomaly is given by:

$$PV = \Delta\psi + \frac{f^2}{N^2}\frac{\partial^2\psi}{\partial z^2}, \tag{4}$$

with ψ the streamfunction, Δ the horizontal Laplacian operator and f and N assumed constant. The relative vorticity ζ is given by $\Delta\psi$. From PV conservation, ζ is related to the stretching term, $\frac{f^2}{N^2}\frac{\partial^2\psi}{\partial z^2}$, via the horizontal divergence as[30,56]:

$$\frac{d\zeta}{dt} = -f\chi\,, \tag{5}$$

$$\frac{f^2}{N^2}\frac{d}{dt}\frac{\partial^2\psi}{\partial z^2} = f\chi \tag{6}$$

with χ the horizontal divergence.

Dynamics in the $k^{-4/3}$ scale range

In the $k^{-4/3}$scale range, KE and APE spectra are equal, which is equivalent to PV $= 0$ (refs)[14,18]. This configuration corresponds to a subset category of the QG framework, referred to as surface quasigeostrophy (SQG)[14–16,18] and initially used by ref[15] to study the dynamics at the Earth's tropopause. Using equations (2) and (3), the streamfunction at the tropopause (where $z = 0$) can be written as:

$$\frac{\partial\psi_T}{\partial z} = \frac{N^2}{f}h = \frac{N^2}{f}H_0\,\tau, \tag{7}$$

with subscript T denoting the tropopause. Integration of PV$= 0$ (eq. 4, valid in the troposphere) using the boundary condition at the tropopause given by equation (7) and assuming that ψ vanishes at $z = -\infty$, leads to the spectral solution:

$$\widehat{\psi}(k,z) = \widehat{\psi}_T \exp\left(k\frac{N}{f}z\right), \tag{8}$$

$$\frac{\partial\widehat{\psi}}{\partial z} = \frac{\partial\widehat{\psi}_T}{\partial z}\exp\left(k\frac{N}{f}z\right). \tag{9}$$

From PV$= 0$ and equations (7), (8) and (9), the relative vorticity at the tropopause can now be linked to the optical depth anomaly τ as:

$$\widehat{\zeta_\tau} + N H_0\,\widehat{\tau}\,k = 0 \tag{10}$$

The SQG framework also allows to infer the aspect ratio between horizontal and vertical scales. Indeed, (8) leads to an e-folding vertical scale given by $k\frac{N}{f}H \sim 1$, with H the depth scale. This indicates that the aspect ratio L/H of a structure is close to $N/f \sim 10$. In other words, the largest vortices in the $k^{-4/3}$ scale range ($\sim$ 1,600 km) have a depth extension of about 160 km, further highlighting their shallow depth extension and therefore their 3-D character.

The value of 1600 km can be interpreted as an upper bound for the size of the baroclinic eddies, which positively depends on the convection's strength[19,27,39]. Indeed, a stronger convection tends to increase the baroclinic spectrum's amplitude ($k^{-4/3}$ slope) but does not change the barotropic spectrum's amplitude (k^{-3} slope) for the small-scales[27,39].

Dynamics in the k^{-3} scale range

On the one hand, APE is associated with the stretching term in the PV expression and is therefore related to the depth dependence of the streamfunction, or what is called the baroclinic mode[57]. On the other hand, KE is associated with the relative vorticity in the PV expression[57]. The exchanges between both energies are driven by the divergence (equations (5) and (6)). APE spectrum in the k^{-3} scale range has a much smaller variance than KE (Fig. 3a) and, in addition, the divergence is small (Fig. 3b) in this range. These two characteristics indicate that the depth dependent contribution (or the baroclinic part) to the total streamfunction is small and therefore that the streamfunction is dominated by the depth-independent part (or the barotropic part)[58]. These arguments imply that vortices are 2-D (depth-independent) in this scale range.

KE and enstrophy transfer

We diagnose the KE and enstrophy (ENS) transfer between wavenumbers in spectral space using the momentum equations at the tropopause (where vertical velocities are null). Multiplying these equations by the conjugate of the horizontal wind speed and without considering dissipation for simplicity's sake, leads to[37,46,59]:

$$\frac{1}{2}\frac{\partial|\widehat{\mathbf{u}_h}|^2}{\partial t} = -\mathrm{Re}\left(\widehat{\mathbf{u}_h}^*.(\widehat{\mathbf{u}_h.\nabla_h\mathbf{u}_h})\right) - \frac{1}{\rho_o}\mathrm{Re}\left(\widehat{\mathbf{u}_h}^*.\nabla_h p\right), \tag{11}$$

$$\frac{1}{2}\frac{\partial|\widehat{\zeta}|^2}{\partial t} = -\mathrm{Re}\left(\widehat{\zeta}^*.(\widehat{\mathbf{u}_h.\nabla_h\zeta})\right) - \mathrm{Re}\left(f\widehat{\zeta}^*.\widehat{\chi}\right), \tag{12}$$

with $.^*$ the complex conjugate and $\mathrm{Re}(.)$ the real part. Equations (11) and (12) are the equations for the time evolution for a given wavenumber k of the KE and ENS, respectively. The first terms on the right hand side of equations (11) and (12) are nonlinear advection terms, whereas the seconds terms are sources and/or sinks.

$$\mathrm{KE}_{\mathrm{adv}}(k) = -\mathrm{Re}\left(\widehat{\mathbf{u}_h}^*.\,(\widehat{\mathbf{u}_h.\nabla_h\mathbf{u}_h})\right), \tag{13}$$

$$\mathrm{ENS}_{\mathrm{adv}}(k) = -\mathrm{Re}\left(\widehat{\zeta}^*.\,(\widehat{\mathbf{u}_h.\nabla_h\zeta})\right). \tag{14}$$

More precisely, the terms (13) and (14) represent the KE and ENS, respectively, gained (lost) by a wavenumber k from (to) other wavenumbers. Fig. 3d, from which the upscale KE transfer is inferred, shows equation (13) in a variance preserving form (i.e., multiplied by k).

Fig 4b shows the enstrophy spectral flux estimated as:

$$\Pi_{\mathrm{ENS}}(k) = \int_k^{k_s} \mathrm{ENS}_{\mathrm{adv}}(k)\,dk, \tag{15}$$

with k the isotropic wavenumber defined previously.

Planetary Burger number

Here, we explore how our results compare with previous modelling studies[8–11], which computed a planetary Burger number $\mathrm{Bu} = L_d^2/2a^2$, with L_d an internal Rossby radius of deformation and a the planetary radius. Using an upper limit value of $L_d = 1600$ km (i.e., the size of the largest baroclinic eddies), yields $\mathrm{Bu} = 2.6\times10^{-4}$, corresponding to a regime with multiple circumpolar cyclones[9,10] and hence comparing favorably with refs[8–11].

Data availability

JIRAM data are available at the Planetary Data System (PDS) online (https://atmos.nmsu.edu/PDS/data/PDS4/juno_jiram_bundle/data_calibrated/). Data products used in this study include: calibrated, geometrically controlled, radiance data mapped onto an orthographic projection centered on the north pole and velocity vectors derived from the radiance data. The raw data used in this study are listed in the Extended Data Table 1. Brightness maps and velocity vectors can be found in the Supplementary Information.

Code availability statement

The code is available upon request to the corresponding author and will shortly be made available on https://github.com/liasiegelman.

Acknowledgements

A portion of this work was carried out at the California Institute of Technology under a contract with the National Aeronautics and Space Administration (NASA), Grant/Cooperative Agreement Number 80NSSC20K0555, and a contract with the Juno mission, which is administered for NASA by the Southwest Research Institute. L.S. was first supported by a Caltech postdoctoral research grant and then by the Scripps Institutional Postdoctoral Program. P.K. was supported by a NASA senior fellowship. A.P.I. is supported by NASA funds to the Juno project and by NSF grant number 1411952. W.R.Y. acknowledges funding from NSF. The JIRAM project is founded by the Italian Space Agency (ASI) through ASI-INAF agreements n. I/010/10/0, 2014-050-R.0, 2016-23-H.0 and 2016-23-H.1-2018. The authors thank three anonymous reviewers for their comments, which help improve the manuscript.

Author Contributions

L.S. and P.K. led the data analysis and data interpretation and drafted the manuscript. S.P.E. processed the infrared brightness maps and wind vectors. A.P.I., S.P.E., W.R.Y. and A.B. contributed to the scientific interpretation of the results. A.M., A.A., D.G., C.P., G.S. provided expertise on the JIRAM instrument. All authors reviewed the manuscript.

Competing interests

The authors declare no competing interests.

Materials and Correspondence

Correspondence and requests for materials should be addressed to Lia Siegelman, lsiegelman@ucsd.edu.

Extended Data Table 1. List of infrared images used in this study

n01a	JIR_IMG_RDR_2017033T114006_V02	n03a	JIR_IMG_RDR_2017033T115620_V02
n01b	JIR_IMG_RDR_2017033T114036_V02	n03b	JIR_IMG_RDR_2017033T115650_V02
n01c	JIR_IMG_RDR_2017033T114107_V02	n03c	JIR_IMG_RDR_2017033T115721_V02
n01d	JIR_IMG_RDR_2017033T114137_V02	n03d	JIR_IMG_RDR_2017033T115751_V02
n01e	JIR_IMG_RDR_2017033T114208_V02	n03e	JIR_IMG_RDR_2017033T115822_V02
n01f	JIR_IMG_RDR_2017033T114238_V02	n03f	JIR_IMG_RDR_2017033T115852_V02
n01g	JIR_IMG_RDR_2017033T114309_V02	n03g	JIR_IMG_RDR_2017033T115923_V02
n01h	JIR_IMG_RDR_2017033T114339_V02	n03h	JIR_IMG_RDR_2017033T115953_V02
n01i	JIR_IMG_RDR_2017033T114410_V02	n03i	JIR_IMG_RDR_2017033T120024_V02
n01j	JIR_IMG_RDR_2017033T114440_V02	n03j	JIR_IMG_RDR_2017033T120054_V02
n01k	JIR_IMG_RDR_2017033T114511_V02	n03k	JIR_IMG_RDR_2017033T120125_V02
n01l	JIR_IMG_RDR_2017033T114541_V02	n03l	JIR_IMG_RDR_2017033T120155_V02

n02a	JIR_IMG_RDR_2017033T114813_V02	n04a	JIR_IMG_RDR_2017033T120426_V02
n02b	JIR_IMG_RDR_2017033T114843_V02	n04b	JIR_IMG_RDR_2017033T120457_V02
n02c	JIR_IMG_RDR_2017033T114914_V02	n04c	JIR_IMG_RDR_2017033T120527_V02
n02d	JIR_IMG_RDR_2017033T114944_V02	n04d	JIR_IMG_RDR_2017033T120558_V02
n02e	JIR_IMG_RDR_2017033T115015_V02	n04e	JIR_IMG_RDR_2017033T120628_V02
n02f	JIR_IMG_RDR_2017033T115045_V02	n04f	JIR_IMG_RDR_2017033T120659_V02
n02g	JIR_IMG_RDR_2017033T115116_V02	n04g	JIR_IMG_RDR_2017033T120730_V02
n02h	JIR_IMG_RDR_2017033T115146_V02	n04h	JIR_IMG_RDR_2017033T120800_V02
n02i	JIR_IMG_RDR_2017033T115217_V02	n04i	JIR_IMG_RDR_2017033T120831_V02
n02j	JIR_IMG_RDR_2017033T115247_V02	n04j	JIR_IMG_RDR_2017033T120901_V02
n02k	JIR_IMG_RDR_2017033T115318_V02	n04k	JIR_IMG_RDR_2017033T120932_V02
n02l	JIR_IMG_RDR_2017033T115348_V02	n04l	JIR_IMG_RDR_2017033T121002_V02

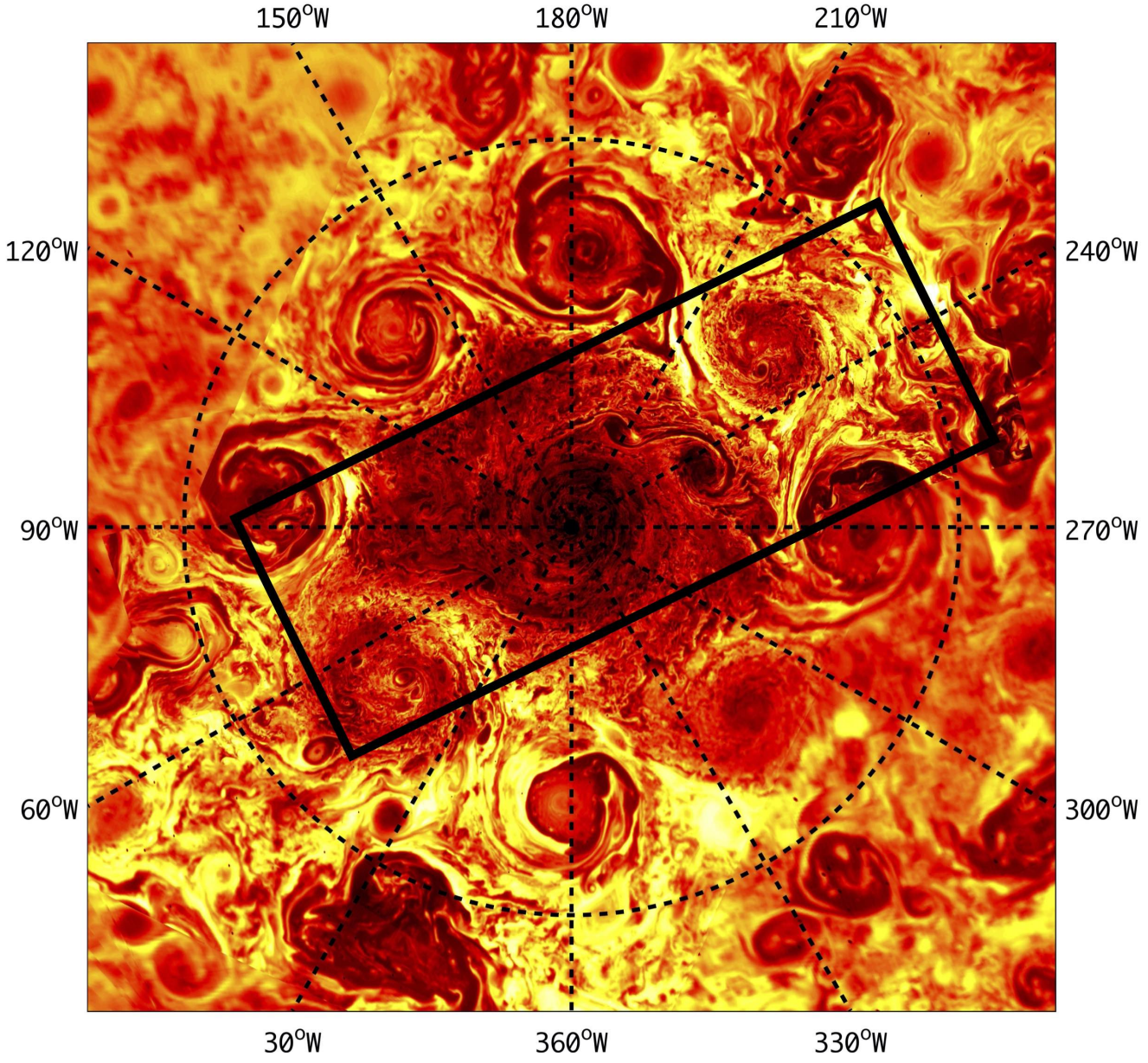

Figure 1. Infrared image of the northern polar region as seen by JIRAM[1] on February 2, 2017 Brightness temperature, corrected for nadir viewing, ranges from 206 K (darkest color) to 227 K (brightest color). The dashed circle at 80°N is about 12,000 km from the pole. The area analyzed in this paper is highlighted by the black rectangle and captures the polar cyclone, parts of the circumpolar cyclones at 45°, 100°, 220° and 260° W, as well as two smaller anticyclones (i.e., the dark features) at 210-240° W, which are joined by a streamer.

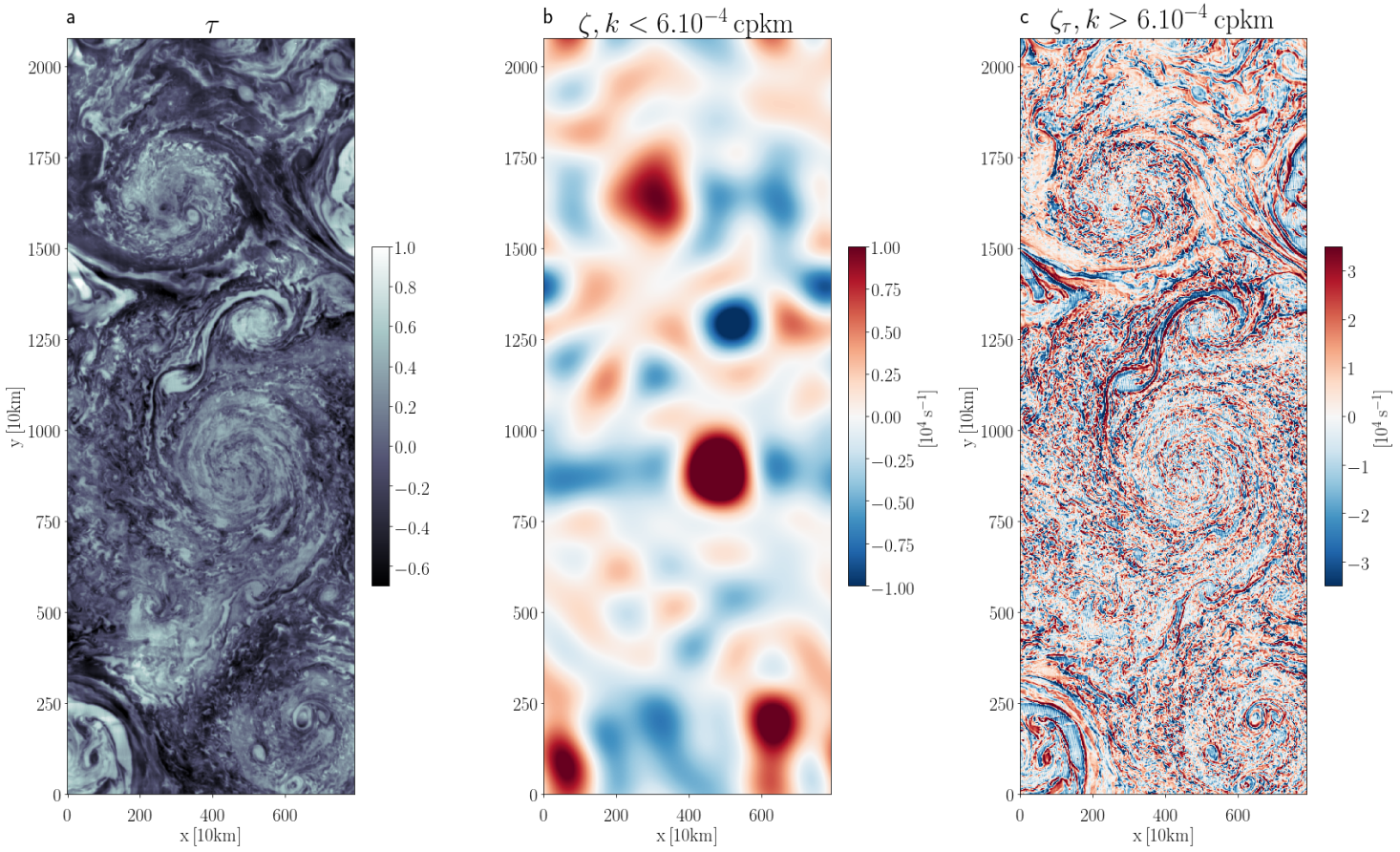

Figure 2. Dynamical context Mosaic of a) optical thickness anomaly τ derived directly from the infrared observations, defined as $\tau = \log(I_0/I) - \overline{\log(I_0/I)}$, with the overbar indicating the domain-average, b) large-scale relative vorticity ζ derived from the wind measurements (Extended Data Fig. 1) after application of a low-pass filter that retains lengthscales greater than 1,600 km (i.e., wavenumbers $k < 6.10^{-4}$ cpkm) and c) small-scale relative vorticity ζ_τ derived from τ after application of a high-pass filter that retains lengthscales smaller than 1,600 km (i.e., wavenumbers $k > 6.10^{-4}$ cpkm, see Methods). As ζ_τ is directly related to cloud thickness, it is the signature of cloud convection. Large-scale vortices in b) gain their energy from small-scale vortices in c) via an upscale energy transfer (see main text).

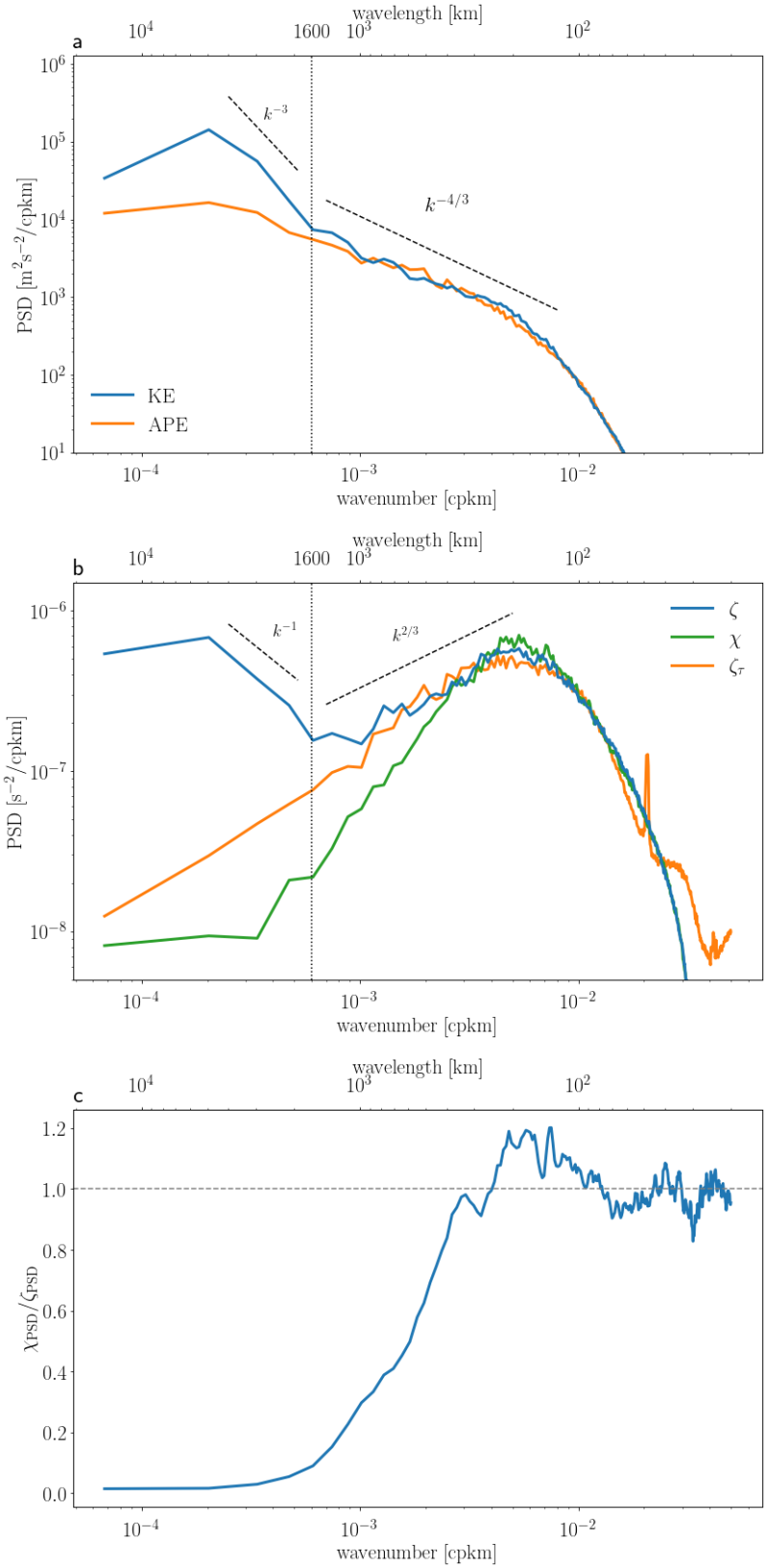

Figure 3. Spectral characteristics a) Spectra kinetic energy (KE, blue curve) and available potential energy (APE, orange curve). b) Power spectra of relative vorticity (ζ, blue curve), horizontal divergence (χ, green curve) and vorticity derived from τ (ζ_τ, orange curve). See Extended Data Fig. 2 for ζ and χ in physical space. A spectral slope discontinuity in KE and ζ occurs at 6.10^{-4} cpkm ($\sim$ 1,600 km), highlighted by the vertical dashed line. Thick dashed lines show spectral slopes. c) χ to ζ power spectra ratio χ_{PSD}/ζ_{PSD}.

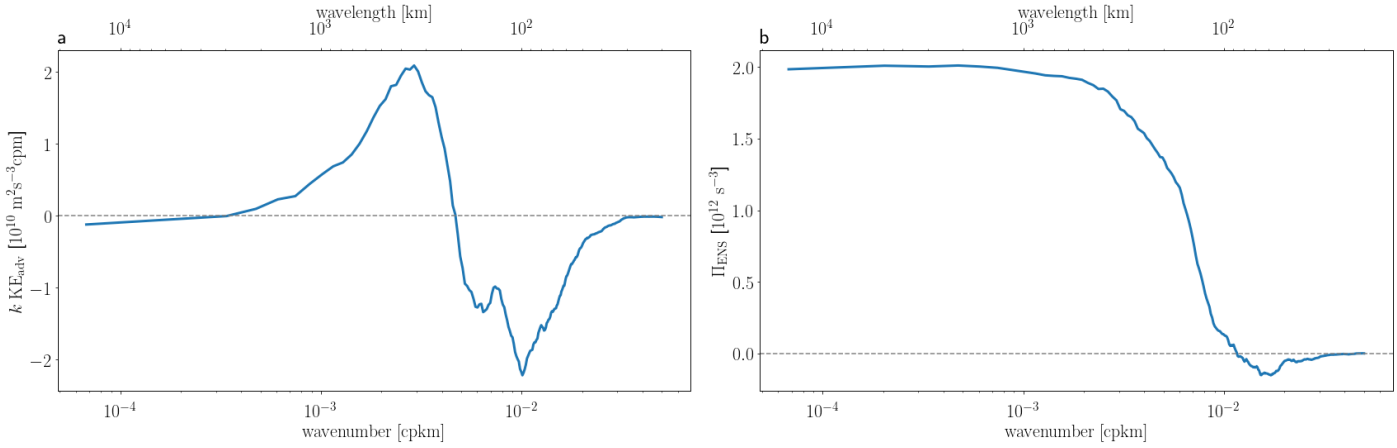

Figure 4. Spectral fluxes derived from the wind measurements a) KE transfer in variance preserving form ($k\,\mathrm{KE_{adv}}$). Positive (negative) $k\,\mathrm{KE_{adv}}$ indicates an energy gain (loss). Scales smaller (larger) than 215 km lose (gain) energy, corresponding to an upscale energy transfer. b) Enstrophy spectral flux (see Methods) showing an ubiquitous direct cascade from large to small scales, consistent with an upscale KE transfer in classical theory of rotating turbulence[37].

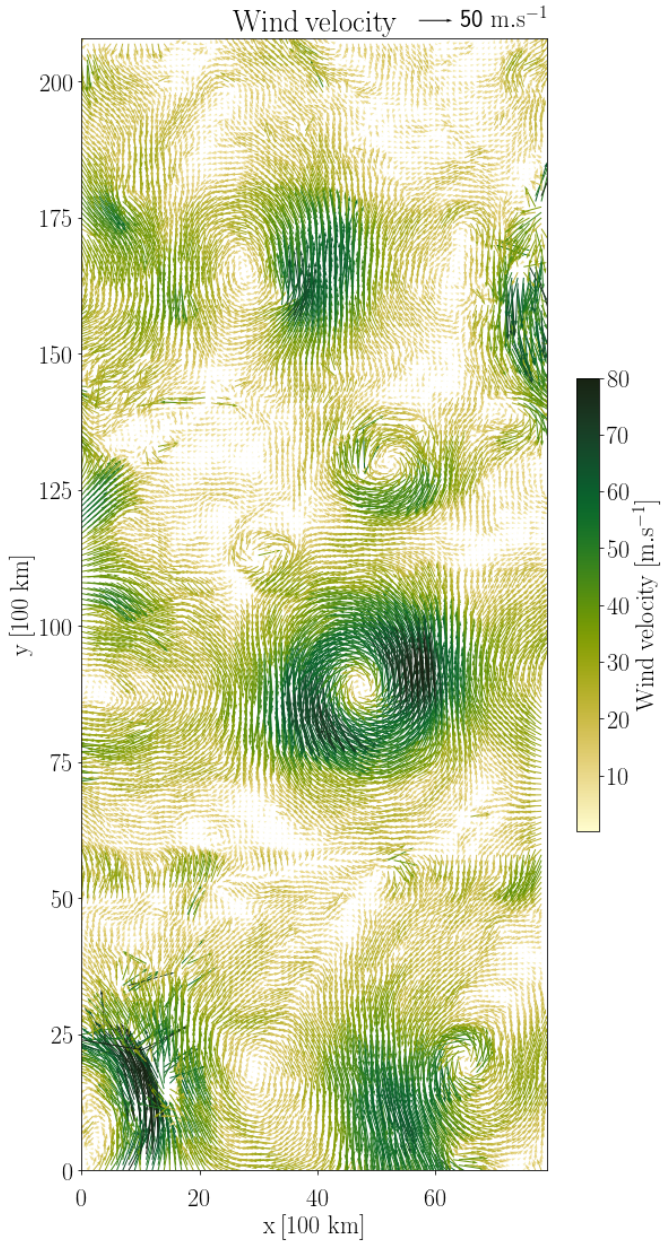

Extended Data Figure 1. Map of wind velocity Map of wind velocity derived by tracking cloud motions in sequences of overlapping infrared images n01 and n03 (see Methods) after application of a butterworth filter of order 2 and cutoff wavelength of 500 km. 1 out of 10 wind speed data point is plotted for visualization purpose. Note that the colorbar is saturated and maximum values reach $\sim$ 120 m s^{-1}.

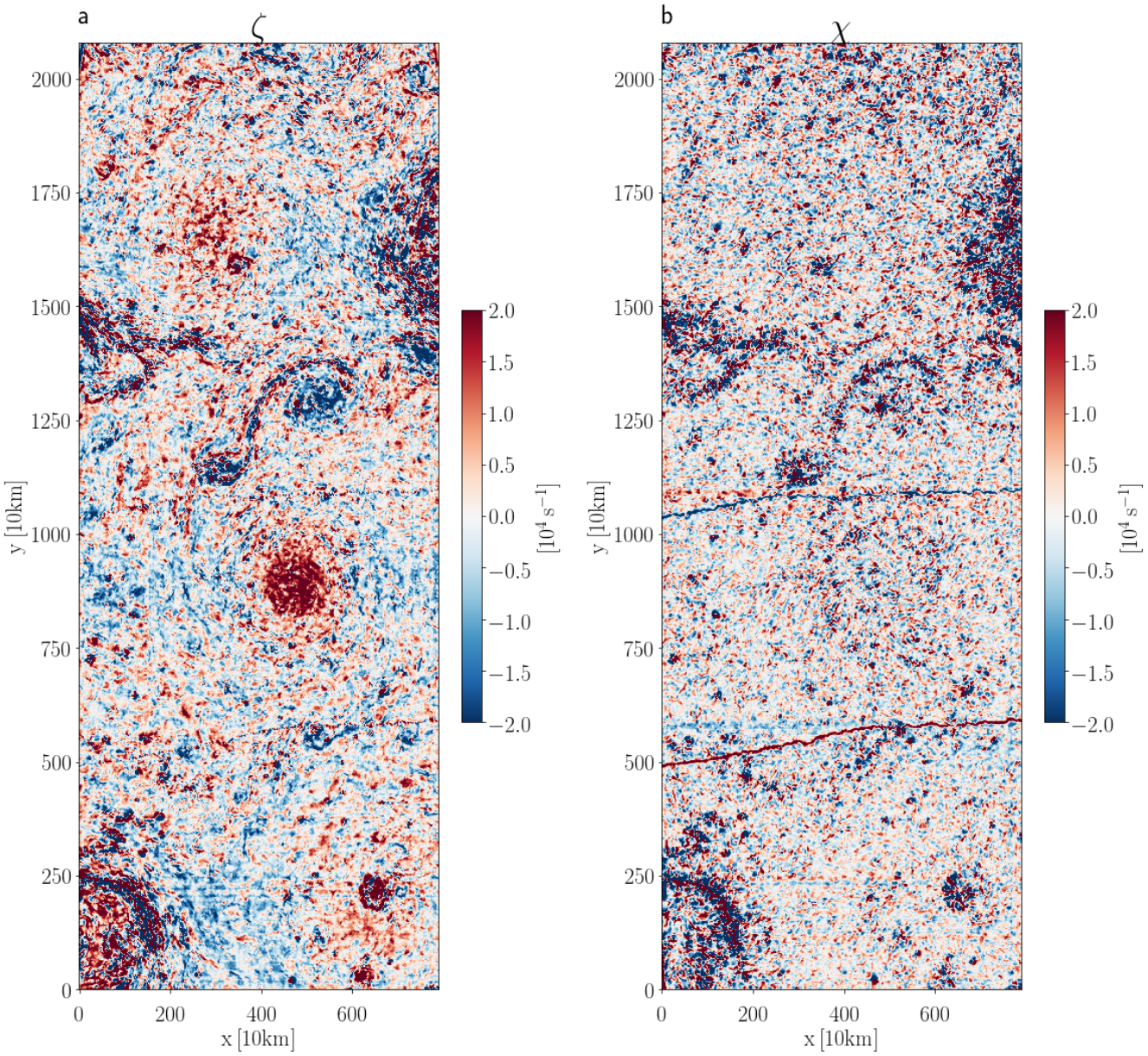

Extended Data Figure 2. Relative vorticity and horizontal divergence Maps of a) relative vorticity ζ and b) horizontal divergence χ corresponding to the spectra shown in Figure 2 b (blue and green curves, respectively). These fields were derived from wind measurements to which a Butterworth filter of order 1 and cutoff lengthscale of 250 km was applied (see Methods and Extended Data Fig. 1). The seams between the mosaic' strips are particularly visible in b).

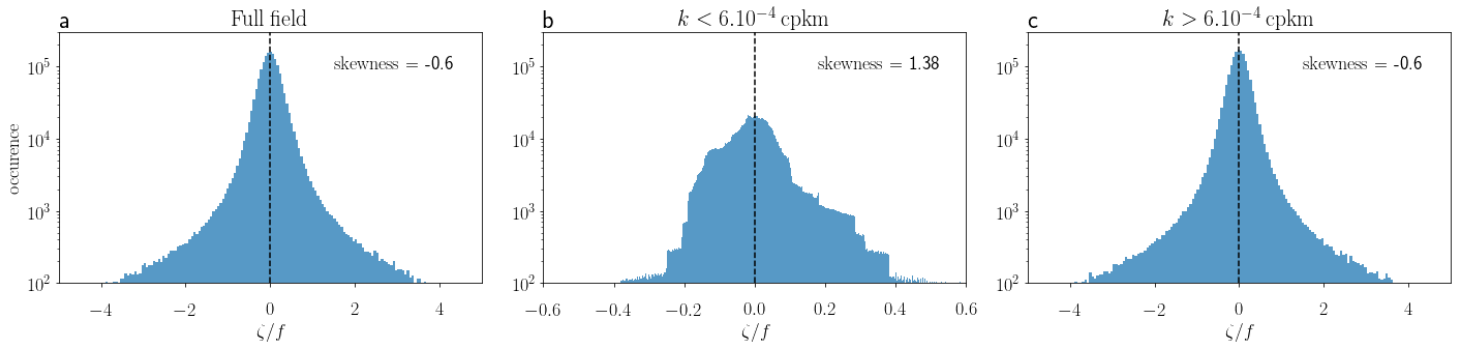

Extended Data Figure 3. Histograms of Rossby number Histograms of Rossby number (Ro$= \zeta/f$) for a) all lengthscales, b) lengthscales $> 1,600$ km (i.e., wavenumbers $< 6.10^{-4}$ cpkm), c) lengthscales $< 1,600$ km (i.e., wavenumbers $> 6.10^{-4}$ cpkm). Ro reaches one for scales $< 1,600$ km, highlighting strong nonlinear interactions (see Methods).

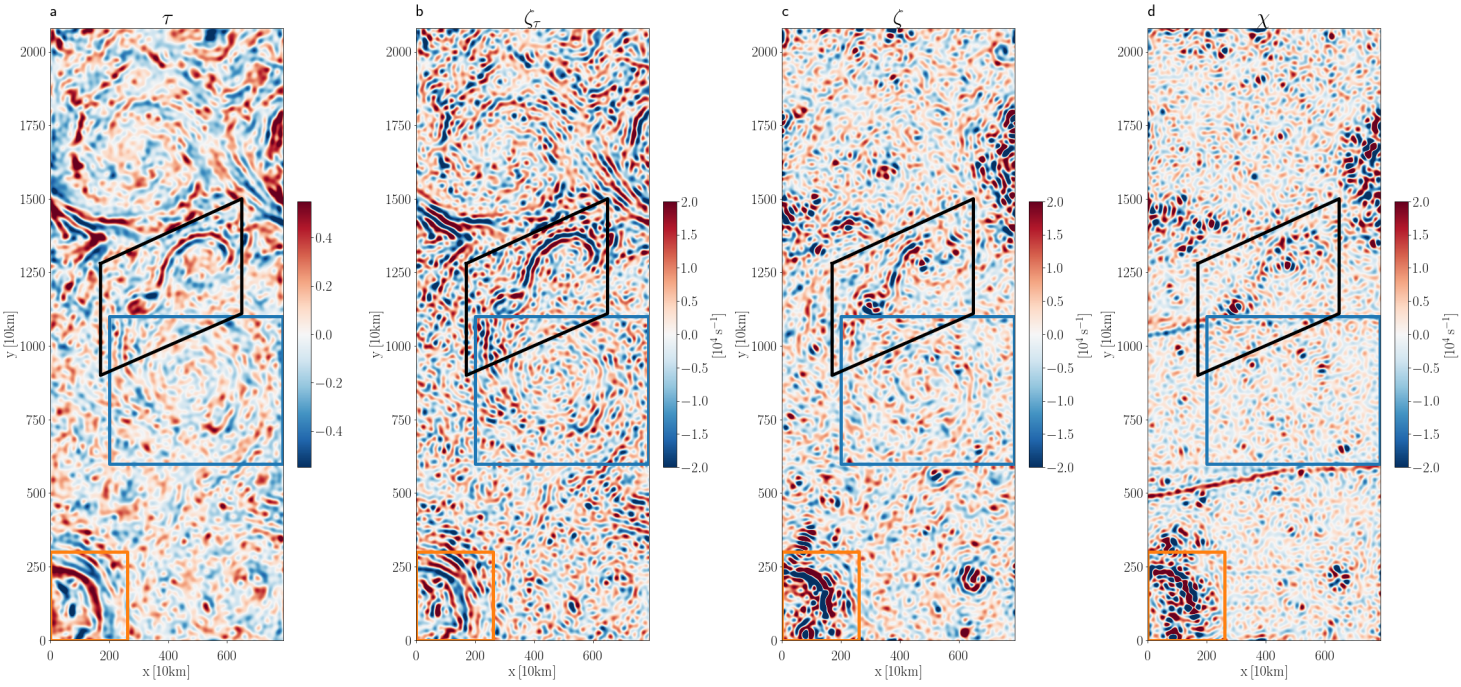

Extended Data Figure 4. Band pass filtered τ, ζ_τ, ζ and χ between 250 and 1,600 km Maps of filtered a) τ, b) ζ_τ, c) ζ and d) χ after application of a band pass filter that retains lengthscales between 250 and 1,600 km (see Methods). The region delineated by the black polygon comprises the streamer subdomain joining two intermediate-scale anticyclones that is discussed in the main text. The blue rectangle comprises the polar vortex and the orange rectangle captures filamentary structures surrounding one of the circumpolar cyclone. These subdomains are analyzed in Extended Data Figs. 5–7.

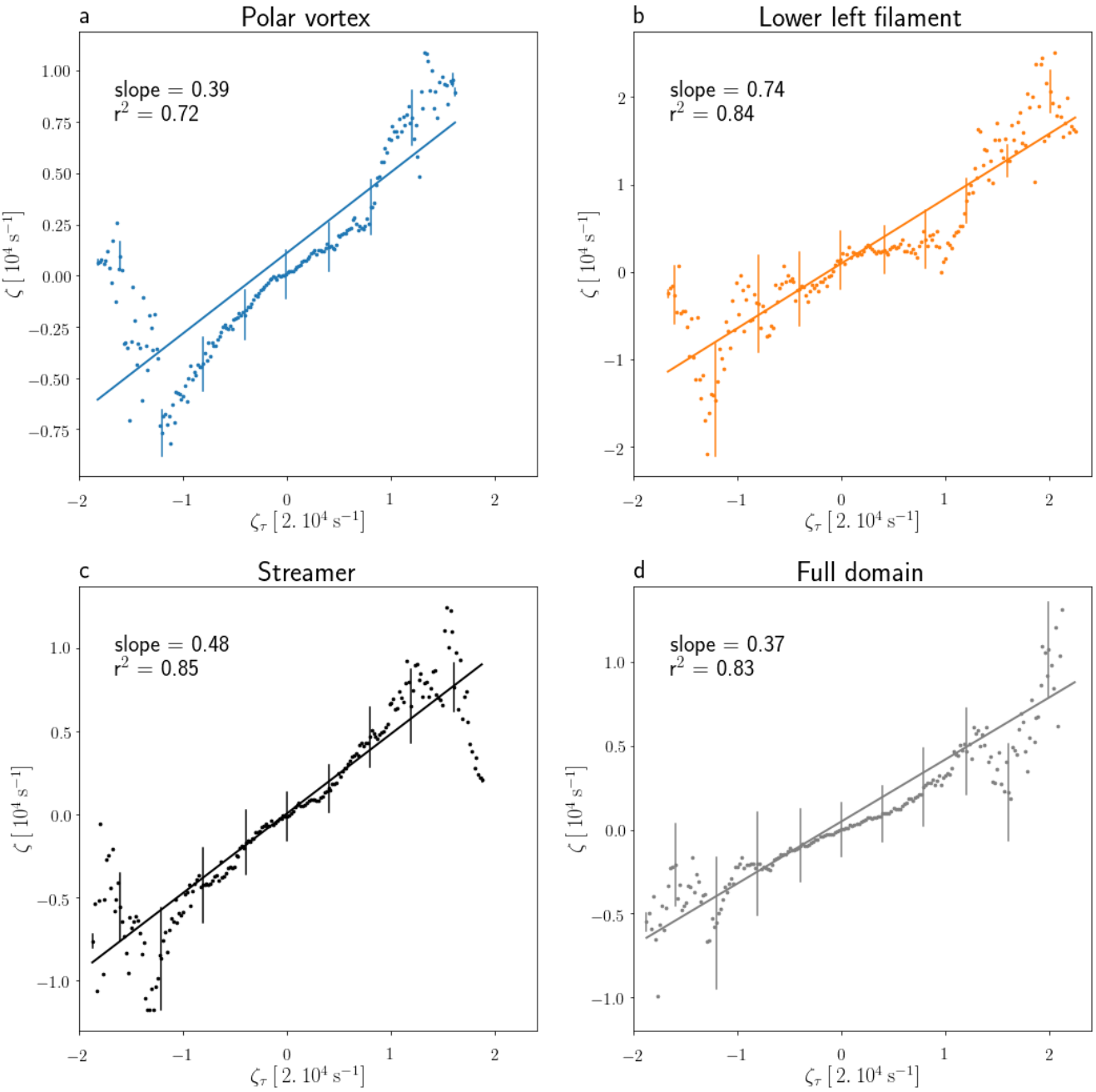

Extended Data Figure 5. Scatter plots between ζ_τ and ζ Scatter plots between ζ_τ and ζ for the fields in Extended Data Fig. 4 per subdomain : in a) the polar vortex (blue rectangle in Extended Data Fig. 4), b) the lower left filament (orange rectangle in Extended Data Fig. 4), c) the streamer subdomain (black polygon in Extended Data Fig. 4), d) the entire domain. Each point represents the average over each grid interval on the abscissa (that has a total of 200 grid intervals), and thin vertical lines show std dev around the averages. Straight lines indicate the least-square regression line between the points. The slope and r^2 of the regression line is shown in each panel.

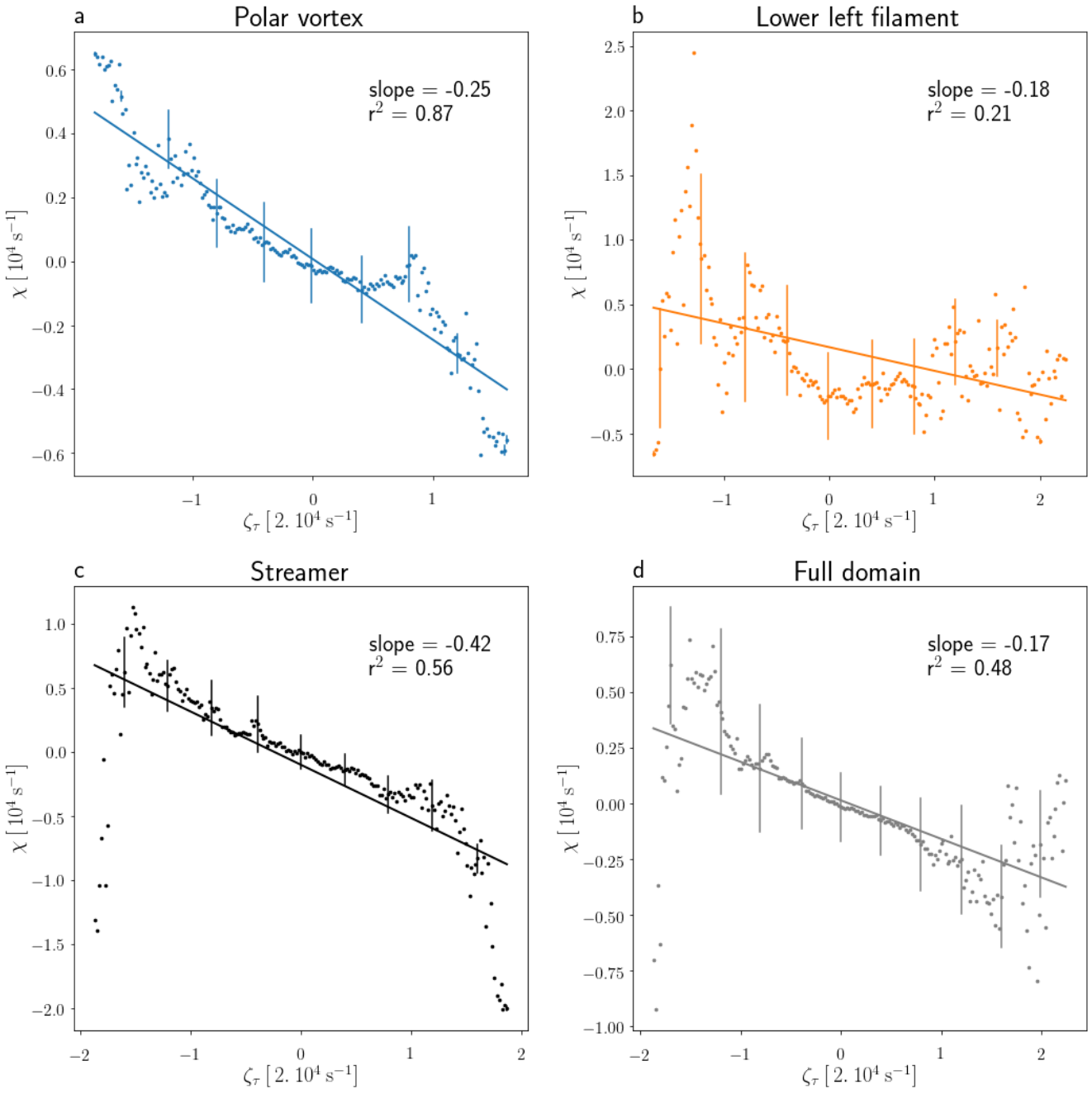

Extended Data Figure 6. Scatter plots between ζ_τ and χ Same as Extended Data Fig. 5 but for χ instead of ζ.

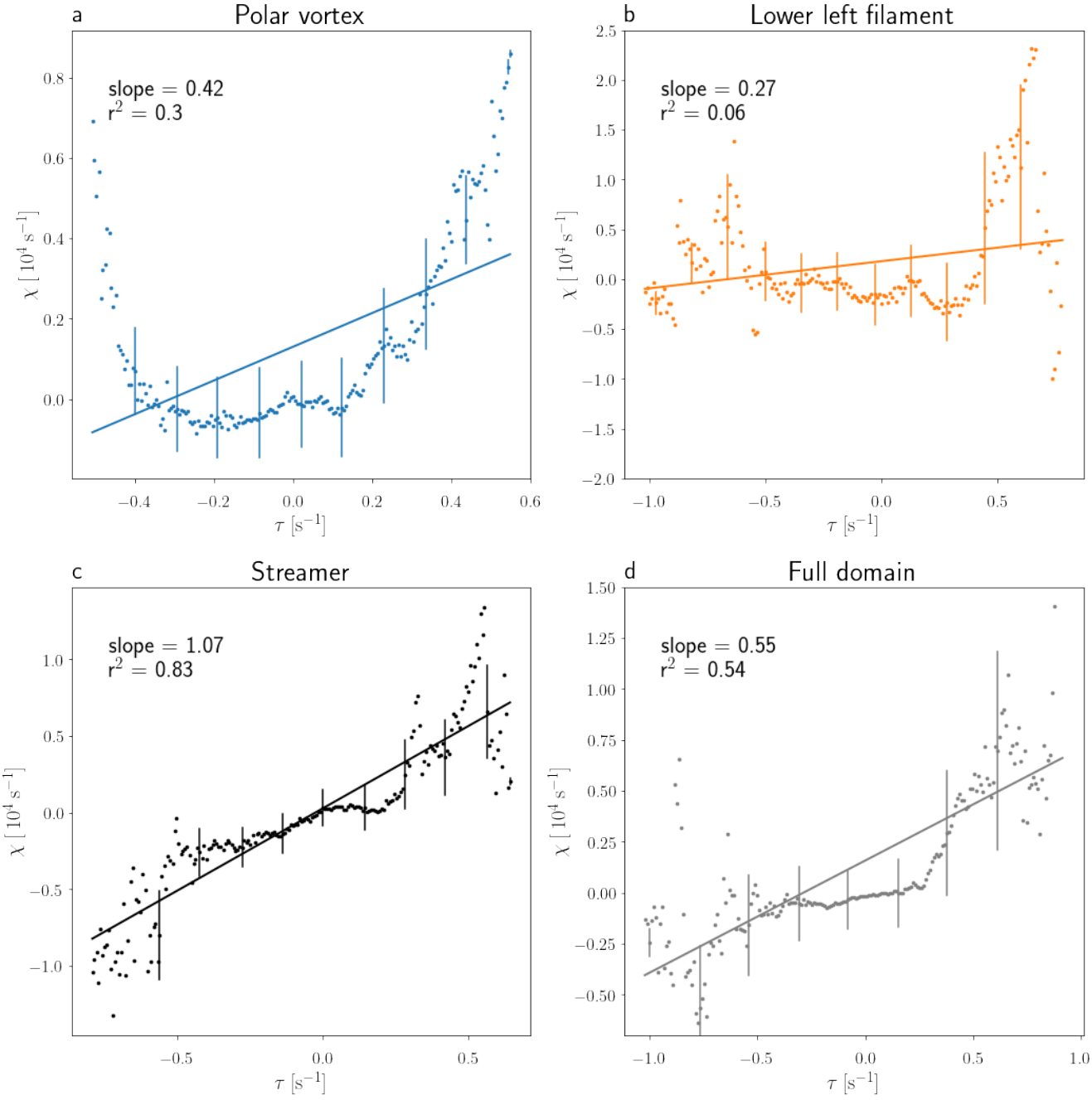

Extended Data Figure 7. Scatter plots between τ and χ Same as Extended Data Fig. 6 but for τ instead of ζ_τ.

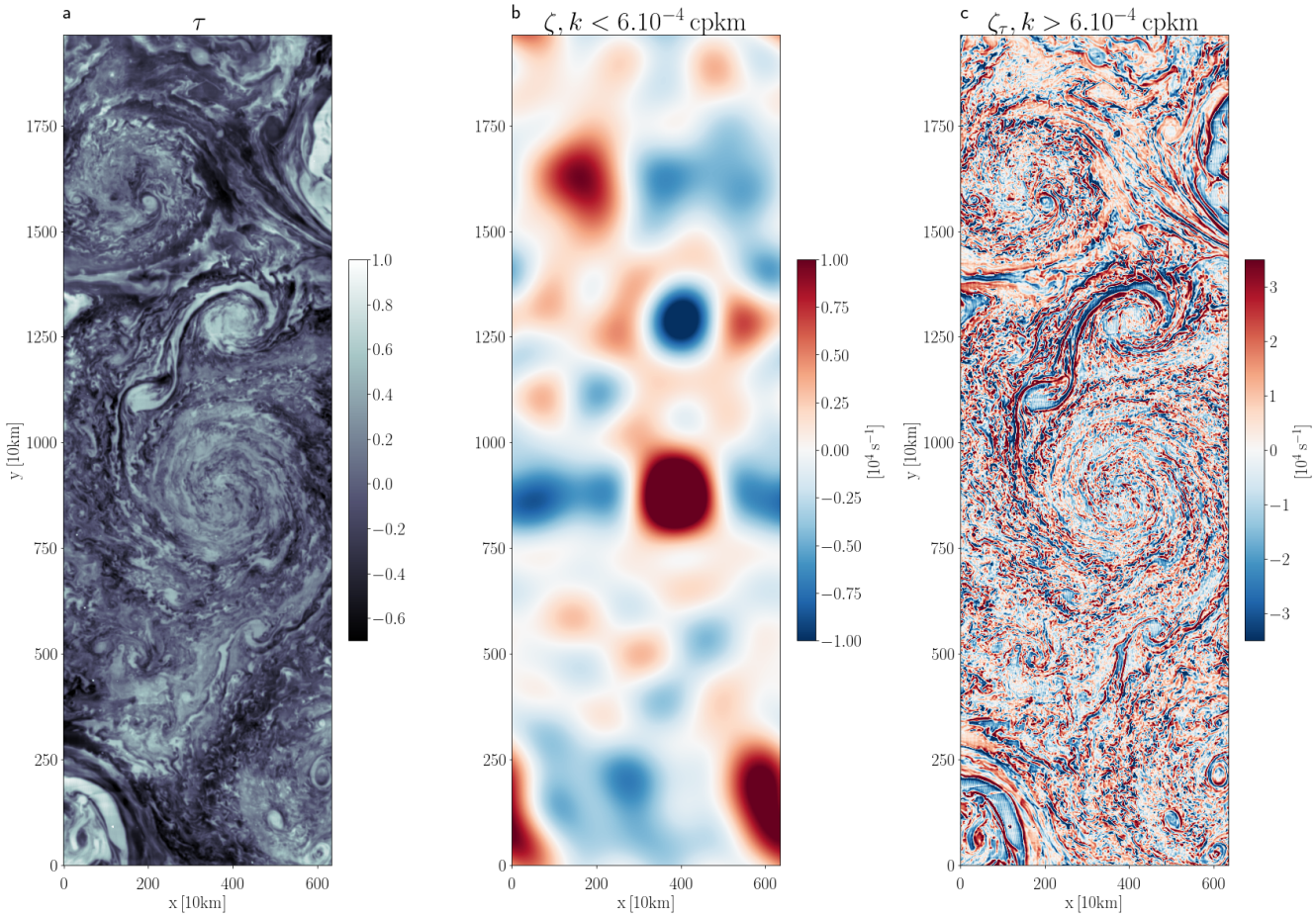

Extended Data Figure 8. Same as Figure 2 but for wind field n0204 and IR image n03

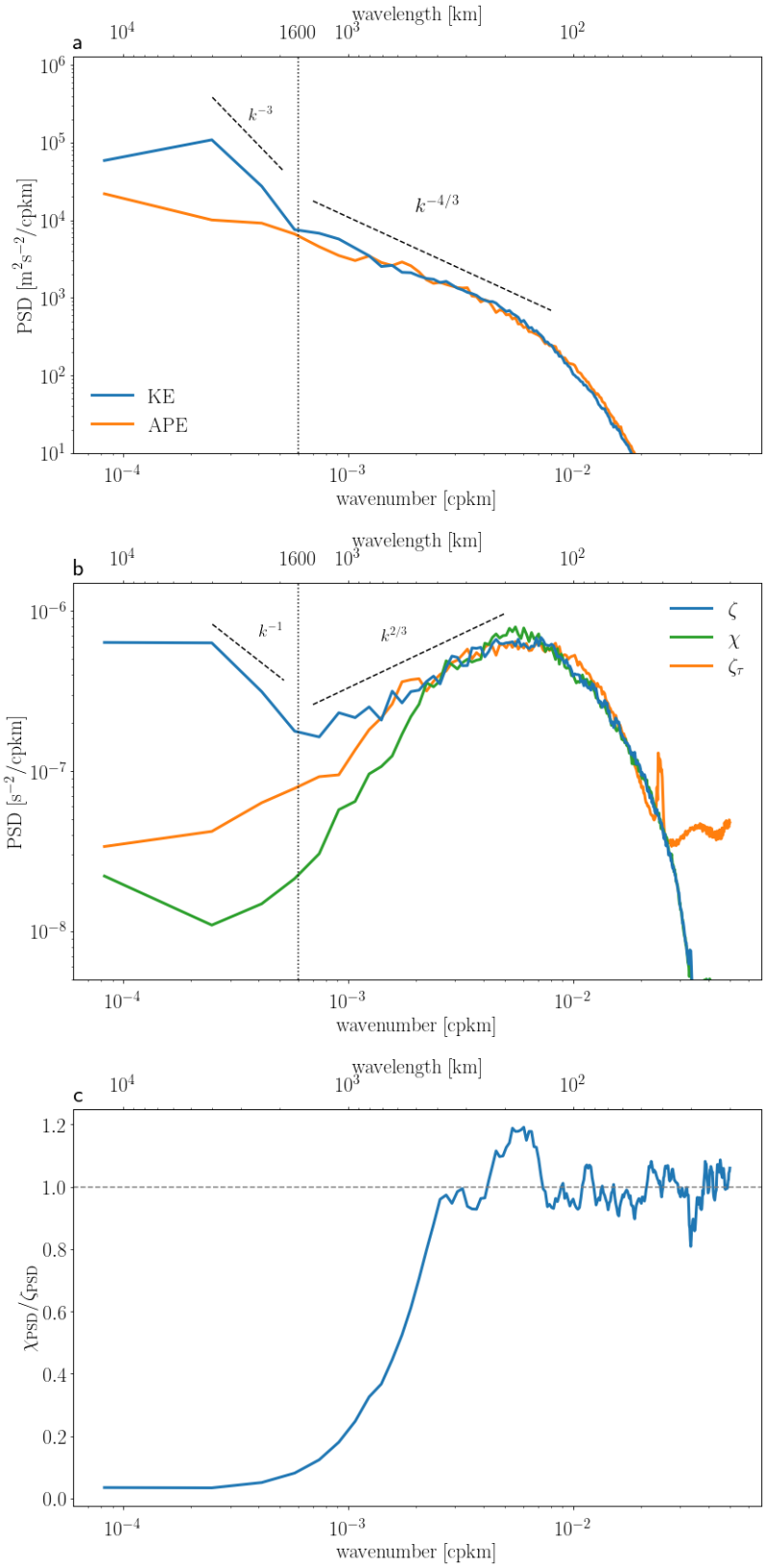

Extended Data Figure 9. Same as Figure 3 but for wind field n0204 and IR image n03

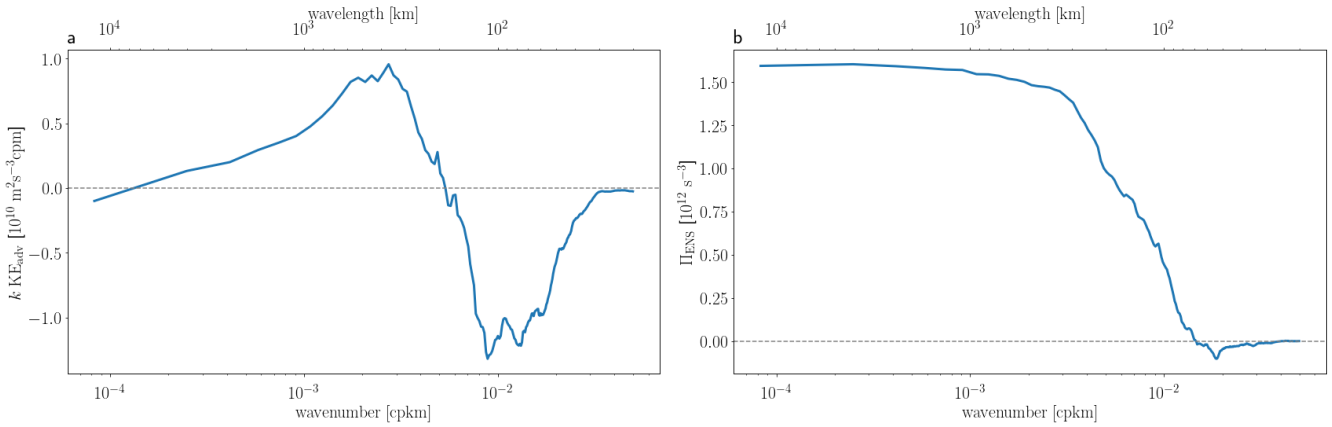

Extended Data Figure 10. Same as Figure 4 but for wind field n0204

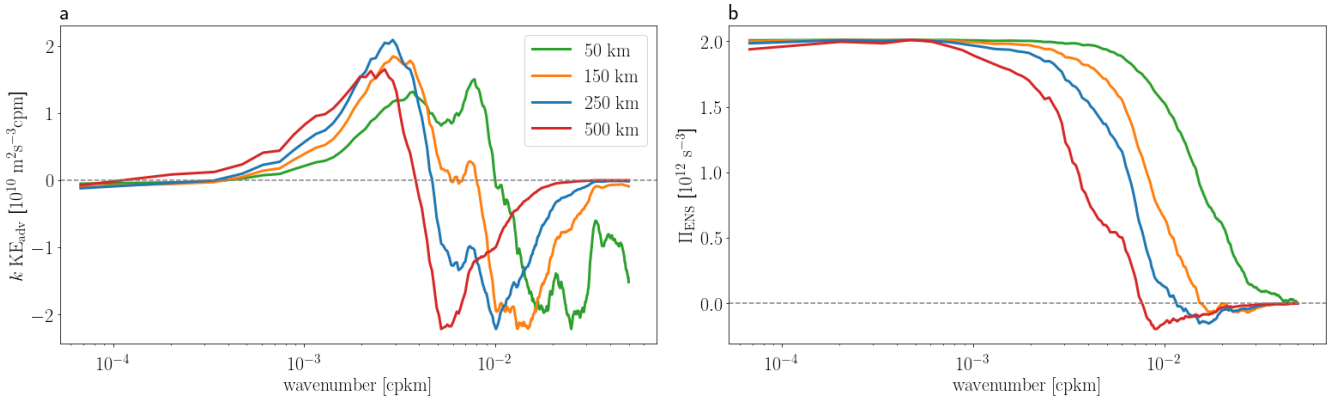

Extended Data Figure 11. Sensitivity of the transfer to the data processing using wind field n0103 a) KE transfer. b) Enstrophy transfer. We varied the cutoff wavelength (different colors) used in the lowpass Butterworth filter of order 1. The inverse KE cascade and direct enstrophy cascade is a robust feature of the flow. However, the zero-crossing is sensitive to the inclusion of small-scales.

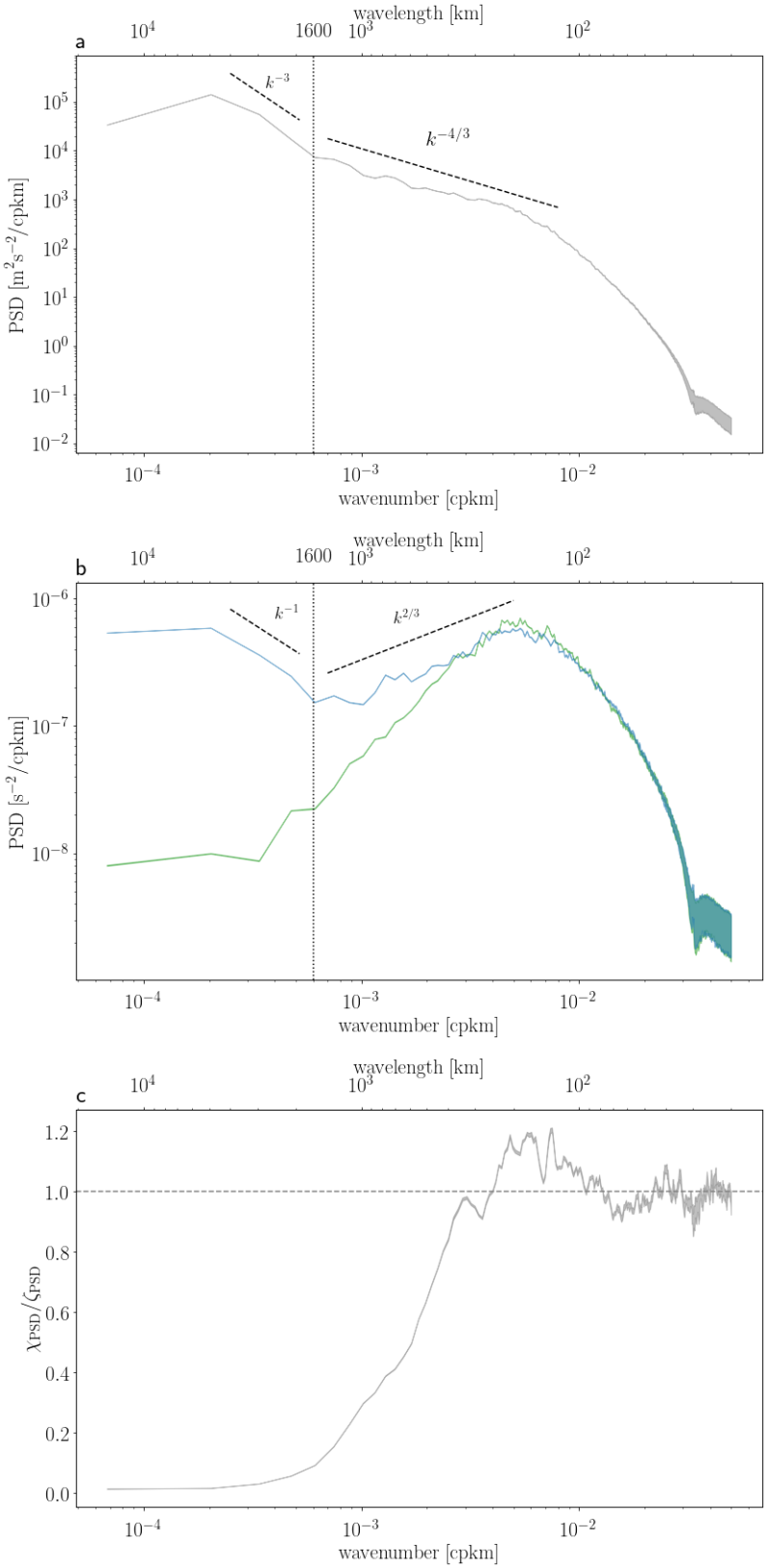

Extended Data Figure 12. Error propagation analysis in wind field n0103. We reproduced Figure 3 with 20 synthetic wind fields equal to n0103 plus an added white noise of standard deviation 2.1 $m.s^{-1}$, corresponding to the error of the wind measurements (see Methods). The figure displays the results' envelope. The error is confined to scales less than ∼50 km, as expected from the steepness of the KE spectrum.

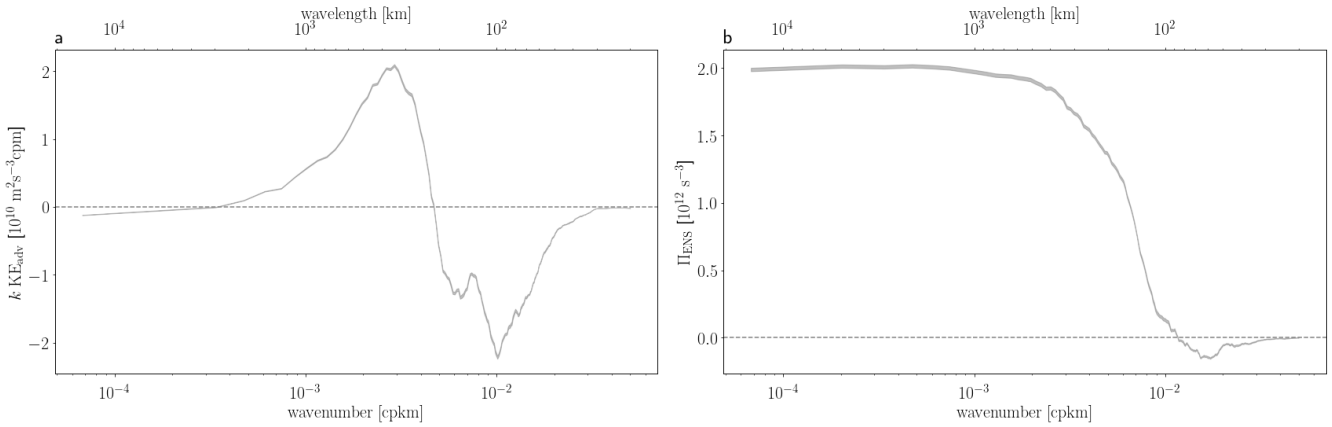

Extended Data Figure 13. Error envelope for a) KE and b) enstrophy transfers using wind field n0103. Same methodology as Extended Data Figure 12 but applied to Figure 4. The error associated with the wind measurements does not impact the transfers computation.